The effect of waves on subgrid-scale stresses, dissipation and model coefficients in the coastal ocean bottom boundary layer

W. A. M. N I M M O S M I T H[1], J. K A T Z[2] A N D T. R. O S B O R N[2,3]

[1]School of Earth, Ocean & Environmental Sciences,
University of Plymouth, Plymouth, Devon, UK

[2]Department of Mechanical Engineering,
The Johns Hopkins University, Baltimore, Maryland, USA

[3]Department of Earth & Planetary Sciences,
The Johns Hopkins University, Baltimore, Maryland, USA

Six sets of particle image velocimetry (PIV) data from the bottom boundary layer of the coastal ocean are examined. The data represent periods of high, moderate and weak mean flow relative to the amplitude of wave-induced motion, which correspond to high, moderate and low Reynolds numbers based on the Taylor microscale (Re_λ). The two-dimensional PIV velocity distributions enable spatial filtering to calculate some of the subgrid-scale (SGS) stresses, from which we can estimate the SGS dissipation, and evaluate the performance of typically used SGS stress models. The previously reported mismatch between the SGS and viscous dissipation at moderate and low Reynolds numbers appears to be related to the sparsity of large vortical structures that dominate energy fluxes.

Conditional sampling of SGS stresses and dissipation based on wave phase using Hilbert transforms demonstrate persistent and repeatable direct effects of large-scale but weak straining by the waves on the SGS energy flux at small scales. The SGS energy flux is phase-dependent, peaking when the streamwise-wave-induced velocity is accelerating, and lower when this velocity is decelerating. Combined with strain rate generated by the mean flow, the streamwise wave strain causes negative energy flux (backscatter), whereas the vertical wave strain causes a positive flux. The phase-dependent variations and differences between horizontal and vertical contributions to the cascading process extend to strains that are substantially higher than the wave-induced motion. These trends may explain the measured difference between spatial energy spectra of streamwise velocity fluctuations and spectra of the wall-normal component, i.e. the formation of spectral bumps in the spectra of the streamwise component at the wavenumbers for the transition between inertial and dissipation scales.

All the model coefficients of typical SGS stress models measured here are phase dependent and show similar trends. Thus, the variations of measured SGS dissipation with phase are larger than those predicted by the model variables. In addition, the measured coefficients of the static Smagorinsky SGS stress model decrease with decreasing turbulence levels, and increase with filter size. The dynamic model provides higher correlation coefficients than the Smagorinsky model, but the substantial fluctuations in their values indicate that ensemble averaging is required. The 'global' dynamic model coefficients indicate that the use of a scale-dependent dynamic model may be appropriate. The structure function model yields poor correlation coefficients

and is found to be over-dissipative under all but the highest turbulence levels. The nonlinear model has higher correlations with measured stresses, as expected, but it also does not reproduce the trends with wave phase.

---

1. Introduction

Large-eddy simulation (LES) has become an increasingly important tool for the study of turbulent transport in atmospheric (e.g. Deardorff 1980; Mason 1989; Shaw & Schumann 1992; Porte-Agel, Meneveau & Parlange 2000) and oceanic flows (e.g. Denbo & Skyllingstad 1996; Skyllingstad *et al.* 1999; Skyllingstad & Wijesekera 2004; Noh, Min & Raasch 2004; Min & Noh 2004; Li, Sanford & Chao 2005). In LES, the Navier–Stokes equations are filtered spatially to give

$$\frac{\partial \tilde{u}_i}{\partial t} + \tilde{u}_j \frac{\partial \tilde{u}_i}{\partial x_j} = -\frac{1}{\rho}\frac{\partial \tilde{p}}{\partial x_i} + \tilde{f}_i - \frac{\partial \tau_{ij}^{SGS}}{\partial x_j} + \nu \frac{\partial^2 \tilde{u}_i}{\partial x_j \partial x_j} \tag{1.1}$$

where a tilde indicates spatial filtering over a scale Δ, $\tilde{f}$ is a body force and τ_{ij}^{SGS} is the subgrid-scale (SGS) stress tensor

$$\tau_{ij}^{SGS} = \widetilde{u_i u_j} - \tilde{u}_i \tilde{u}_j. \tag{1.2}$$

The SGS stresses must be modelled based on parameters of the filtered (resolved) velocity field, typically the resolved velocity gradient tensor, $\partial \tilde{u}_i/\partial x_j$. Development of models is normally based on the evolution equation for the filtered kinetic energy, $0.5\tilde{u}_i^2$ (Pope 2000),

$$\frac{\partial \frac{1}{2}\tilde{u}_i\tilde{u}_i}{\partial t} + \tilde{u}_j \frac{\partial \frac{1}{2}\tilde{u}_i\tilde{u}_i}{\partial x_j} = \frac{\partial}{\partial x_i}\left[\tilde{u}_j\left(2\nu\tilde{S}_{ij} - \tau_{ij}^{SGS} - \frac{\tilde{p}}{\rho}\delta_{ij}\right)\right] - 2\nu\langle\tilde{S}_{ij}\tilde{S}_{ij}\rangle - \varepsilon^{SGS} + \tilde{f}_i\tilde{u}_i \tag{1.3}$$

where $\tilde{S}_{ij} = 0.5(\partial \tilde{u}_i/\partial x_j + \partial \tilde{u}_j/\partial x_i)$ is the filtered strain rate, δ_{ij} is the Kronecker delta, and ε^{SGS} is the so-called SGS dissipation rate, defined as

$$\varepsilon^{SGS} = -\tau_{ij}^{SGS}\tilde{S}_{ij}. \tag{1.4}$$

It represents transfer of energy from the resolved to subgrid scales and is sometimes referred to as production of SGS energy. Consequently, most of the attempts to model the SGS stresses have focused on reproducing the correct levels of SGS dissipation. Unlike viscous dissipation, ε^{SGS} can be either positive or negative. A positive value indicates flux of energy from resolved scales to small (subgrid) scales whereas a negative value indicates 'backscatter' of energy from small to large scales. The mean SGS dissipation, representing the balance between positive and negative fluxes, is typically positive in turbulent flows. Reviews on this subject are provided by Lesieur & Metais (1996), Piomelli (1999) and Meneveau & Katz (2000).

In recent years, we have developed a submersible planar particle image velocimetry (PIV) system for measuring the flow structure and turbulence in the bottom boundary layer of the coastal ocean (Bertuccioli *et al.* 1999; Doron *et al.* 2001; Nimmo Smith *et al.* 2002, 2004). PIV measures the instantaneous distributions of two velocity components in a sample area, which can be spatially filtered and used for evaluating SGS stress models, and for estimating the SGS dissipation for LES (e.g. Liu, Meneveau & Katz 1994; Liu, Katz & Meneveau 1999; Meneveau & Katz 1999; Tao, Katz & Meneveau 2002; Chen, Katz & Meneveau 2005; Chen, Meneveau & Katz 2006).

When the spatial filter scale falls in the inertial subrange of isotropic homogeneous turbulence, the mean ensemble-averaged SGS dissipation, $\langle \varepsilon^{SGS} \rangle$, is (almost) equal to the total viscous dissipation rate (Lilly 1967; Pope 2000). This agreement has been observed in oceanic PIV data with mean currents that are significantly larger than the amplitude of the wave-induced motion (Doron *et al.* 2001; Nimmo Smith *et al.* 2005). However, at low Taylor-microscale Reynolds numbers, which are not uncommon in the bottom boundary layer of the coastal ocean, Nimmo Smith *et al.* (2005, hereafter referred to as NS05) find that $\langle \varepsilon^{SGS} \rangle$ is substantially lower than the viscous dissipation, $\langle \varepsilon^V \rangle$. This result is consistent with results of numerical simulations by Piomelli *et al.* (1991), which show that near the wall of low-Reynolds-number channel flows, $\langle \varepsilon^{SGS} \rangle$ is small and can even be negative. Owing to the growing application of LES for modelling of oceanic flows, it would be useful to examine trends of the SGS dissipation in the bottom boundary layer in detail. What makes coastal flows unique is the combination of mean currents (e.g. tidal flows) and oscillatory wave-induced motion, which is generated either by local winds or transported as swells from events located far from a test site (e.g. Snodgrass *et al.* 1966). Thus, turbulence in the coastal bottom boundary layer is subjected both to shear that characterizes any boundary layer, and to periodic wave-induced straining. In this paper, we show that even weak wave-induced straining has substantial impact on the SGS dissipation. We subsequently evaluate the behaviour and response to waves of typically used SGS stress models, such as the commonly used eddy viscosity models, including the Smagorinsky model with fixed coefficients, the dynamic Smagorinsky model, the structure function model, as well as the nonlinear model. Brief background on each of these models is provided in the following sections.

1.1. *Dissipation estimates and SGS stress models*

To evaluate ε^{SGS} (or its various models) from PIV data one needs to make assumptions on the missing out-of-plane components. As in NS05 we have the option to follow Liu *et al.* (1994) and assume that the missing terms involving shear stress (and strains) are equal to the available measured values ($\tau_{13}\tilde{S}_{13} = \tau_{12}\tilde{S}_{12} = \tau_{23}\tilde{S}_{23}$). Such assumptions are only valid for an ensemble average of homogeneous isotropic flow. Furthermore, we also assume that the missing normal stress terms are averages of the available normal stress components, i.e. $\tau_{22} = 0.5(\tau_{11} + \tau_{33})$. The missing normal strain term can be determined using the continuity equation, i.e. $\tilde{S}_{22} = -(\tilde{S}_{11} + \tilde{S}_{33})$. The resulting estimate for the SGS dissipation is

$$\varepsilon^{SGS} = -\tau_{ij}\tilde{S}_{ij} \approx -\frac{1}{2}(\tau_{11}\tilde{S}_{11} + \tau_{33}\tilde{S}_{33} - \tau_{11}\tilde{S}_{33} - \tau_{33}\tilde{S}_{11} + 12\tau_{13}\tilde{S}_{13}). \qquad (1.5)$$

However, these assumptions are unreliable since the turbulence in the bottom boundary layer is anisotropic (NS05). Consequently, to evaluate stress models we opt to rely only on the available in-plane components, i.e. using

$$\varepsilon^{SGS}_{2D} = -(\tau_{11}\tilde{S}_{11} + \tau_{33}\tilde{S}_{33} + 2\tau_{13}\tilde{S}_{13}). \qquad (1.6)$$

Both values are provided for comparison, but only ε^{SGS}_{2D} is used for testing models.

The PIV data extend to wavenumbers in the dissipation/viscous range enabling us to obtain estimates of the viscous dissipation, based on instantaneous velocity gradients, for comparison to the SGS dissipation. As in NS05, Doron *et al.* (2001)

and Luznik *et al.* (2007*a*), the 'direct' estimate of the viscous dissipation rate is

$$\varepsilon^V \approx 4\nu \left\langle \left(\frac{\partial u}{\partial x}\right)^2 + \left(\frac{\partial w}{\partial z}\right)^2 + \frac{3}{4}\left(\frac{\partial u}{\partial z}\right)^2 + \frac{3}{4}\left(\frac{\partial w}{\partial x}\right)^2 + \left(\frac{\partial u}{\partial x}\frac{\partial w}{\partial z}\right) + \frac{3}{2}\left(\frac{\partial u}{\partial z}\frac{\partial w}{\partial x}\right) \right\rangle$$

(1.7)

where ν is the kinematic viscosity of the water and $\langle\rangle$ indicates ensemble averaging. In NS05 (and see table 1 below) we show that, because the vector spacing (δ) is 4 to 10 times larger than the Kolmogorov scale ($\eta = (\nu^3/\varepsilon)^{1/4}$) this method underestimates the actual dissipation rate by 25 % to 45 %. These underestimates increase with Re_λ, the Taylor-microscale Reynolds number. Similar trends have been observed recently by Luznik *et al.* (2007*a*) by fitting the PIV data to the universal dissipation spectrum and comparing the resolved and missing part of the spectrum.

1.1.1. *Smagorinsky model*

The popular Smagorinsky eddy viscosity model (Smagorinsky 1963; Lilly 1967) for the deviatoric part of the SGS stress tensor ($= \tau_{ij}^{SGS} - (1/3)\tau_{kk}^{SGS}\delta_{ij}$) is

$$\tau_{ij}^S = -2(c_S\Delta)^2|\tilde{S}|\tilde{S}_{ij}$$

(1.8)

where $|\tilde{S}| = \sqrt{2\tilde{S}_{ij}\tilde{S}_{ij}}$ is the strain magnitude and c_S is the (static) Smagorinsky coefficient that has to be determined. To calculate the strain magnitude ($|\tilde{S}|$) using two-dimensional PIV data, we adopt the two-dimensional surrogate (as in the dissipation rate), i.e.

$$\tilde{S}_{ij}\tilde{S}_{ij} = \tilde{S}_{11}\tilde{S}_{11} + \tilde{S}_{33}\tilde{S}_{33} + 2\tilde{S}_{13}\tilde{S}_{13}.$$

(1.9)

In a non-uniform grid the Smagorinsky model should be modified to (Scotti, Meneveau & Lilly 1993)

$$\tau_{ij}^S = -2(c_S F(a_1, a_2)\Delta_{eq})^2|\tilde{S}|\tilde{S}_{ij}$$

(1.10)

where $\Delta_{eq} = (\Delta_1\Delta_2\Delta_3)^{1/3}$ is the equivalent grid size and

$$F(a_1, a_2) = \cosh\sqrt{\tfrac{4}{27}[(\ln(a_1))^2 - \ln(a_1)\ln(a_2) + (\ln(a_2))^2]}$$

(1.11)

is a known function of the two grid aspect ratios ($a_1 = \Delta_2/\Delta_1$, $a_2 = \Delta_3/\Delta_1$). Using two-dimensional PIV, $a_1 = 1$ and a_2 is the filter size divided by the light sheet thickness (see table 1).

The value of c_S is determined by matching ε^{SGS} (equation (1.6)) to the modelled dissipation, ε^S, where

$$\varepsilon^S = -\tau_{ij}^S\tilde{S}_{ij}.$$

(1.12)

Using only the deviatoric part of the stress,

$$c_S^2 = \frac{\langle\varepsilon_{2D}^{SGS}\rangle}{[\Delta_{eq}F(a_1, a_2)]^2\langle|\tilde{S}|^3\rangle},$$

(1.13)

where here the ensemble averaging is taken as the 'global' mean of all data in any particular data series. Inherently, based on its definition, ε^S is always positive, only allowing energy flux from resolved to subgrid scales. Traditionally, $c_S = 0.16$ (Lilly 1967), but results of simulations show that the optimal value of c_S decreases with increasing mean shear (Porte-Agel *et al.* 2000) and values as low as $c_S = 0.065$ have been used in simulations of channel flow (Moin & Kim 1982). It has also been observed that the Smagorinsky coefficient decreases with increasing anisotropy in both the resolved and SGS velocities (Horiuti 1993).

1.1.2. *Dynamic model using the Germano identity*

It is well known that a constant coefficient in the (static) Smagorinsky model is not appropriate in complex flows (e.g. Meneveau & Katz 1999), and consequently Germano *et al.* (1991) proposed a dynamic Smagorinsky model to determine the model coefficient locally from the resolved scales. A test filter at scale $\alpha\Delta$ (typically $\alpha = 2$) is adopted and the static model coefficient (c_S^2) is replaced by one determined locally (c_D^2) using (Lilly 1992)

$$c_D^2 = \frac{\langle L_{ij} M_{ij} \rangle}{\langle M_{ij} M_{ij} \rangle} \qquad (1.14)$$

where $L_{ij} = \overline{\widetilde{u_i \widetilde{u}_j}} - \overline{\widetilde{u}}_i \overline{\widetilde{u}}_j$ and $M_{ij} = -2\Delta^2(\alpha^2 \overline{|\widetilde{S}|} \, \overline{\widetilde{S}}_{ij} - \overline{|\widetilde{S}|\widetilde{S}_{ij}})$, and an overbar denotes filtering at a scale $\alpha\Delta$. Very importantly for a self-consistent *a priori* analysis, the second filtering only employs spatially averaged data, as sampled on a grid of mesh size Δ. Here, the ensemble averaging is typically done over spatial domains of statistical homogeneity to smooth out sharp fluctuations of the coefficient. It should also be noted that this method relies on a presumption of scale-invariance, i.e. $c_D^\Delta = c_D^{\alpha\Delta}$ (Meneveau & Katz 2000). To resolve scale-dependent trends, Porte-Agel *et al.* (2000) introduce a scale-dependent dynamic model. The dynamically determined model coefficient, and hence the dynamically modelled subgrid dissipation ε^D, can be either positive or negative. During implementation, spatial averaging of the coefficients usually removes negative values which may cause backscatter-induced numerical instabilities. Remaining negative values may then also be clipped at zero.

1.1.3. *Structure function model*

The structure function model of Metais & Lesieur (1992) is commonly used in LES of oceanic flows (e.g. Skyllingstad *et al.* 1999; Skyllingstad & Wijesekera 2004; Li *et al.* 2005). By providing a fit between the resolved turbulence structure and an assumed Kolmogorov turbulent kinetic energy (TKE) spectrum at subgrid scales, the modelled SGS stress is

$$\tau_{ij}^{SF} = -2K_m \widetilde{S}_{ij} \qquad (1.15)$$

where $K_m = 0.063\Delta[\bar{F}(\boldsymbol{x})]^{1/2}$ and $\bar{F}(\boldsymbol{x})$ is the velocity second-order structure function, approximated by

$$\bar{F}(\boldsymbol{x}) = \langle |u_i(x_i) - u_i(x_i + r_i)|^2 \rangle_{|r_i| = \Delta}. \qquad (1.16)$$

In this case, the averaging operator is performed over all the coarse-grid points.

The modelled eddy viscosity is determined locally, as with the dynamic model, and is non-zero only if resolved-scale motions have small-scale variability. As highlighted by Piomelli (1999), the structure function model is actually a Smagorinsky-like model with the strain rate replaced by the velocity gradient tensor when an isotropic grid is used. As with the static Smagorinsky model and unlike the dynamic model, the structure function model is inherently limited to positive dissipation. This model may also be excessively dissipative, particularly in sheared flows (Piomelli 1999).

1.1.4. *Nonlinear model*

The final SGS stress model that we will test is the first-order approximation of the similarity model, the nonlinear model. This model exhibits much better correlation with experimental laboratory data than the static Smagorinsky model (Leonard 1974;

Liu *et al.* 1994; Borue & Orszag 1998; Tao *et al.* 2002) and is given by

$$\tau_{ij}^{NL} = C_{NL}\Delta^2 \tilde{A}_{ik}\tilde{A}_{jk} = C_{NL}\Delta^2 \frac{\partial \tilde{u}_i}{\partial x_k}\frac{\partial \tilde{u}_j}{\partial x_k} \qquad (1.17)$$

where the coefficient, C_{NL}, is also determined by comparing the measured (ε^{SGS}) and modelled ($\varepsilon^{NL} = -\tau_{ij}^{NL}\tilde{S}_{ij}$) SGS dissipation. Unlike the Smagorinsky model, the nonlinear model does allow backscatter of energy, making it prone to numerical instabilities since it overpredicts the backscatter in some cases (Tao *et al.* 2002). A plausible compromise has been the use of a mixed model, involving both nonlinear and eddy viscosity components. For this model, the nonlinear term dominates the stress magnitude, whereas the eddy viscosity term ensures a smooth dissipative behaviour.

1.1.5. *Implementation of SGS models with two-dimensional PIV data*

Consistent with the procedures and terminology used in Liu *et al.* (1994) and Tao *et al.* (2002) we use a box (top hat) filter to calculate the filtered velocity field, i.e.

$$\tilde{u}(x_1, x_2) = \int_{-\infty}^{\infty}\int_{-\infty}^{\infty} u_i(x_1', x_2')F_\Delta(x_1 - x_1', x_2 - x_2')\,dx_1'\,dx_2' \quad (i = 1, 2), \qquad (1.18)$$

$$F_\Delta(x_1, x_2) = \begin{cases} K_1 & \text{if } |x_1| < \Delta/2 \text{ and } |x_2| < \Delta/2 \\ 0 & \text{otherwise} \end{cases}$$

where K_1 is a constant which ensures that the integral of the filter equals unity. In this paper we use $\Delta_1 = \Delta_2 = \Delta$ of 4, 8 and 16 vector spacings based on the availability of data ($\delta = 1/64$ of the sample-area width indicated in table 1). The larger filter scales fall within the inertial range of the velocity spectra for these data, before the spectral roll-off at dissipation scales (e.g. figure 13). However, the smallest filter scale ($\Delta/\delta = 4$) may cover insufficient subgrid scales as discussed further in §3.1. In calculating the parameters based on the gradients of the filtered velocity field (e.g. strain rate) we use a coarse grid, consistent with the data that would be available during LES. However, to increase the database, we repeat the analysis by displacing the coarse grid by δ. Centre finite differencing at a scale of Δ is used for calculating the gradients. Although centre differencing at 2Δ is a more appropriate approach, we opt to use differencing at Δ in our analysis owing to the substantial loss of valuable data resulting from the edge effects of the coarser differencing. The impact of this choice on the magnitudes of coefficients and mean SGS dissipation has been found to be small and does not justify the loss of data.

2. Experimental setup, deployments and data

2.1. *Apparatus*

An extensive description of the present version of the PIV system, as well as details of the data processing methodology, can be found in Nimmo Smith *et al.* (2002, 2004, 2005), and only a brief outline follows. A schematic of the submerged components of the PIV system is shown in figure 1. Dual-exposure images are recorded by a pair of 2K × 2K digital cameras operating at up to 3.3 Hz. Directional ambiguity is overcome by shifting the image vertically within the hardware between exposures. The system comprises two separate sample areas, light sheets and cameras to increase the total sample size. They are essential for calculating the Reynolds shear stresses using structure functions (Trowbridge 1998; Nimmo Smith *et al.* 2002; Luznik *et al.* 2007*b*). For the analysis of SGS stresses, we only use data from one sample area. The
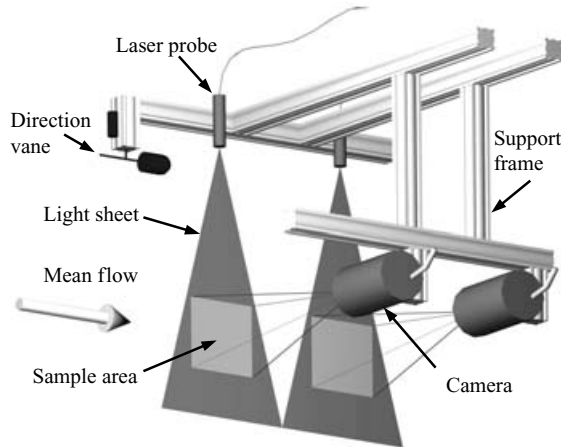
FIGURE 1. A three-dimensional schematic of the submerged components of the PIV system. The scale of the sample areas is given in table 1.

cameras and laser probes are mounted via a turntable to a stable seabed profiling platform, which enables us to align the sample areas with the mean flow direction (determined using a direction vane monitored by a video camera), and to vary the elevation from close to the seabed up to 10 m above the bottom.

Velocity distributions can be extracted using auto-correlation analysis of small windows within the images and detailed calibration information. Constrained by the natural particle concentration, we use 64×64 pixel interrogation windows and 50 % overlap between windows. Thus, each vector map consists of a maximum of 63×63 velocity vectors. The data quality varies depending on the concentration, size and spatial distribution of particles. Provided that the interrogation window contains 5–10 particle pairs, the uncertainty in velocity is estimated conservatively at 0.3 pixels. With a typical displacement of 20 pixels between pulses, the uncertainty of a single velocity vector is 1.5 %. Typically, 60 %–80 % of the vectors satisfy the accuracy criteria of the data analysis software (Roth, Mascenik & Katz 1999; Roth & Katz 2001). Instantaneous velocity distributions that contain less than 60 % vectors are discarded. Gaps within the remaining velocity data are filled by linear interpolation using the vectors located in the direct neighbourhood of a missing vector. A recursive process follows which fills the gaps surrounded by the most 'good' vectors first. The outermost two strips of vectors in each map are discarded since they have been found to be less reliable. Figure 2 shows two sample instantaneous velocity distributions of the same area, recorded one second apart. Here the average instantaneous mean velocity has been subtracted from each vector to highlight the turbulent structures in this flow.

2.2. *Deployments and characterization of data*

Six sets of field data are used in this paper. They were collected during two field deployments off the eastern seaboard of the United States in 2000 and 2001 and are described in detail by NS05. Table 1 gives details of the measurement locations, sampling durations and elevations above the seabed, mean flow speeds for each sampling period ($\langle u_{map} \rangle$, $\langle w_{map} \rangle$), where the subscript 'map' indicates spatial averaging over the entire sample area, and the r.m.s. values of the time series of u_{map} and w_{map} (denoted by u_{map}^{rms}, w_{map}^{rms}), which are dominated by the wave motions. The mean

$u_{map} = 12.4\,\mathrm{cm\,s^{-1}}$, $w_{map} = -0.2\,\mathrm{cm\,s^{-1}}$ ___ $1\,\mathrm{cm\,s^{-1}}$ $u_{map} = 10.6\,\mathrm{cm\,s^{-1}}$, $w_{map} = -0.3\,\mathrm{cm\,s^{-1}}$
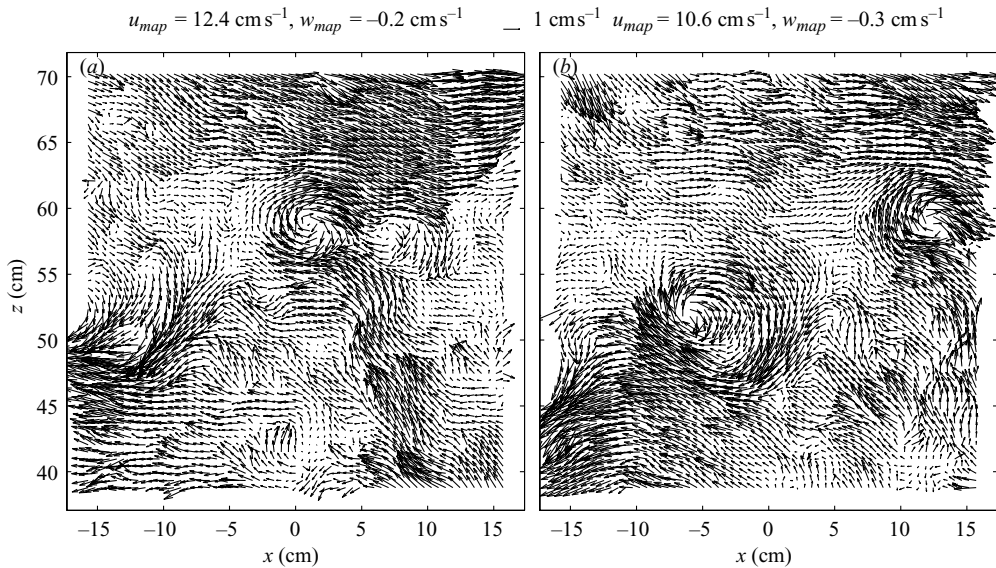

FIGURE 2. Two velocity vector maps of the same area from run D, sampled 1 s apart. The instantaneous mean velocity of the sample area (shown at the top of each map) is subtracted from each vector to highlight the turbulence structure. The vertical coordinates represent the actual distance from the bottom.

vertical shear of the horizontal velocity is also given for each data series, as is the Taylor-microscale turbulent Reynolds number (Re_λ).

Runs A and B, recorded inside the harbour of refuge at the mouth of Delaware Bay in 11 m deep water, are characterized by strong tidal currents and relatively weak wave motion. The seabed at this location consists of coarse sand and broken shell without any ripples or other notable bed forms and the water column was unstratified. Here, Re_λ is in the 350–500 range, which qualifies as a high turbulence level. Runs C to F are recorded at the LEO-15 site off the New Jersey coast, in 21 m deep water, and are characterized by weaker tidal currents and exposure to the oceanic swell. At this site, the seabed consists of coarse sand with ripples having wavelength of approximately 50 cm and heights less than 10 cm. The water column was strongly stratified with a sharp thermocline situated about 7 m above the well-mixed layer closer to the seabed. For runs C and D the mean flow is of the same order as the amplitude of the oscillatory wave-induced motion, and Re_λ is 84–85, indicating a moderate turbulence level. Runs E and F are recorded during periods of very low mean flow, when the oscillatory wave motion dominates, and the turbulence level is also very weak ($Re_\lambda = 29-39$). In NS05 we show spatial turbulent energy spectra for all the data, which in each case indicate that the turbulence is close to isotropic at the largest scales resolved by the instantaneous velocity distributions, but becomes increasingly anisotropic at smaller scales (see also figure 13 that shows compensated spectra for runs C and E). We also observe that the high and moderate turbulence level flows contain large-scale vortical structures, which are advected by the mean currents (e.g. figure 2 is from run D). These structures are found to occur intermittently, but dominate the contributions to the Reynolds shear stress. In weak flows, which do not contain these structures (runs E and F), the shear stresses are essentially zero.

Run	A	B	C	D	E	F	Lab
Date	20 May 2000		9 Sep 2001		10 Sep 2001		
Start Time (UTC -5h)	0240:00	0304:30	0604:00	0339:30	0159:00	0259:00	
Site	Delaware Bay		LEO-15				
Size of square sample (cm)	50.2		34.65				10.00
Vector spacing δ (mm)	7.84		5.41				1.56
Light sheet thickness (mm)	3.5		2.5				1.0
Sampling duration (frames)	1000		4000		2400		550
Sampling frequency (Hz)	3.33		3.33		2.00		
Elevation of centre of sample (cm)	144	35	257	55	245	55	
$\langle u \rangle$ (cm s^{-1})	38.2	32.6	14.9	7.7	-0.5	0.9	
u_{map}^{rms} (cm s^{-1})	3.4	4.5	5.7	4.2	5.1	4.0	
$\langle w \rangle$ (cm s^{-1})	-0.8	-0.3	-0.8	-0.2	0.1	-0.1	
w_{map}^{rms} (cm s^{-1})	1.8	1.5	1.0	0.4	0.9	0.2	
$\langle \partial u/\partial z \rangle$ (s^{-1})	0.040	0.132	0.017	0.027	0.007	0.004	
$\langle \partial w/\partial z \rangle$ (s^{-1})	-0.006	-0.003	-0.001	-0.006	-0.002	-0.003	
$\langle \partial u/\partial x \rangle$ (s^{-1})	0.012	0.006	0.005	0.005	0.001	0.003	
$\langle \partial w/\partial x \rangle$ (s^{-1})	0.014	0.020	0.001	0.002	0.001	-0.001	
$\nu \times 10^6$ (m^{2}s^{-1})	1.18		1.25				1.00
η (mm)	0.63	0.60	1.06	1.06	1.21	1.23	0.20
λ (cm)	2.34	2.63	1.93	1.91	1.49	1.31	0.92
Re_λ	361	490	85	84	39	29	558
$\langle \varepsilon^V \rangle \times 10^6$ (m^2 s^{-3})	10.7	12.4	1.53	1.55	0.914	0.856	666
$\langle \varepsilon^{SGS} \rangle (4\delta) \times 10^6$ (m^{2}s^{-3})	1.21	10.2	0.007	0.036	0.003	-0.005	736
$\langle \varepsilon^{SGS} \rangle (8\delta) \times 10^6$ (m^{2}s^{-3})	3.08	18.5	0.059	0.110	0.009	-0.005	878
$\langle \varepsilon^{SGS} \rangle (16\delta) \times 10^6$ (m^{2}s^{-3})	6.15	27.3	0.115	0.179	0.014	-0.005	873
$\langle \varepsilon_{2D}^{SGS} \rangle (4\delta) \times 10^6$ (m^{2}s^{-3})	0.059	5.66	0.008	0.027	0.007	-0.003	644
$\langle \varepsilon_{2D}^{SGS} \rangle (8\delta) \times 10^6$ (m^{2}s^{-3})	0.986	9.80	0.033	0.066	0.011	-0.006	769
$\langle \varepsilon_{2D}^{SGS} \rangle (16\delta) \times 10^6$ (m^{2}s^{-3})	3.64	14.2	0.049	0.098	0.012	-0.010	827

TABLE 1. Summary statistics of the data sets selected for this paper. Values in parentheses, e.g. (8δ), indicate the filter size.

As a reference, table 1 also provides details of some laboratory data of locally isotropic turbulence generated using four symmetrically positioned rotating grids (Friedman & Katz 2002; Chen *et al.* 2005). This laboratory data set will be used for comparison with the field data in some of the following analysis.

3. Results

3.1. *Trends in SGS and viscous dissipation*

Figure 3(*a*) shows the instantaneous velocity distribution of figure 2(*b*) filtered at $\Delta/\delta = 8$. Smearing of the small-scale structures due to spatial filtering is evident; however the two large vortices are preserved. The corresponding SGS stress and filtered strain components are presented in figures 3(*c*) and 3(*d*) respectively. The distribution of SGS dissipation estimated using equation (1.5) is shown in figure 3(*b*). The distributions of modelled stresses (figure 3*e–h*) will be examined later in §3.3. It is clear that regions of high strain do not coincide with regions of high stress, in agreement with previous observations using laboratory data (Liu *et al.* 1994),
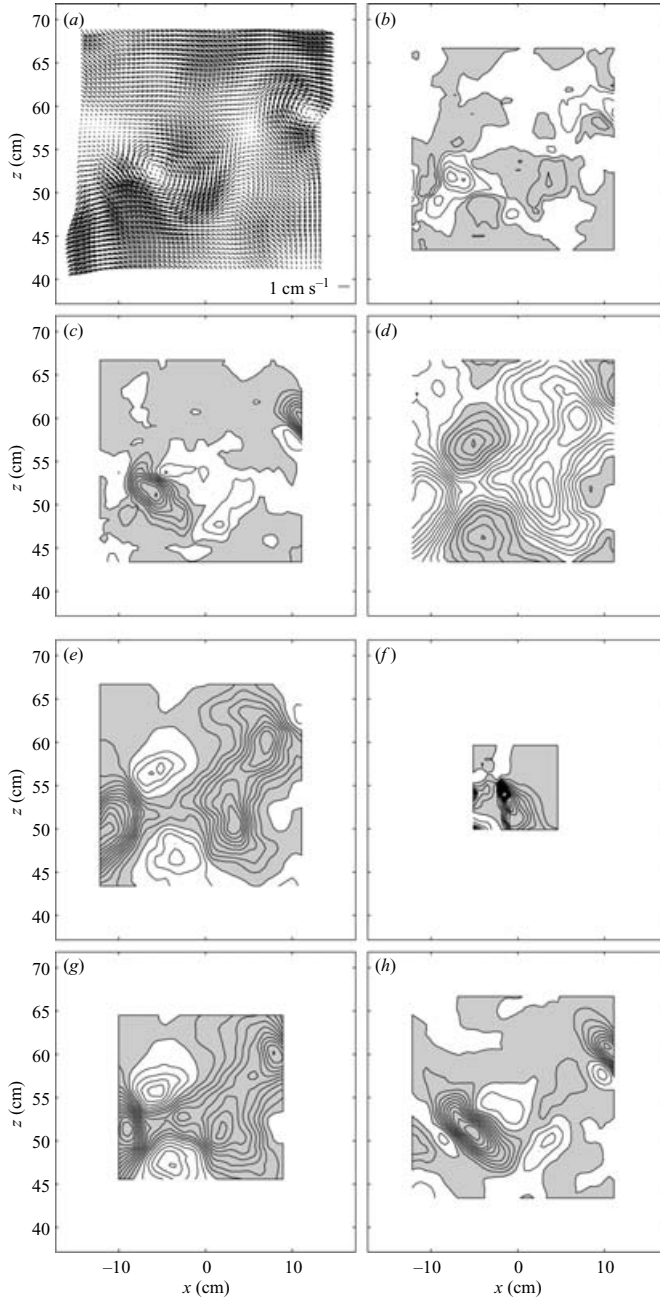
FIGURE 3. (*a*) Instantaneous distribution of the velocity field shown in figure 2(*b*) filtered at $\Delta = 8\delta$, with a reference scale in the bottom right. Corresponding distributions of: (*b*) ε^{SGS} contoured at intervals of $4 \times 10^{-6}\,\mathrm{m^2\,s^{-3}}$; (*c*) τ_{13}^{SGS} contoured at intervals of $5 \times 10^{-6}\,\mathrm{m^2\,s^{-2}}$; (*d*) $\tilde{S}_{13}$ contoured at intervals of $2 \times 10^{-2}\,\mathrm{s^{-1}}$. Sections (*e–h*) are the modelled SGS stresses for the same velocity field: (*e*) τ_{13}^{S} contoured at intervals of $2 \times 10^{-7}\,\mathrm{m^2\,s^{-2}}$, using $c_S = 0.135$; (*f*) τ_{13}^{D} contoured at intervals of $1 \times 10^{-5}\,\mathrm{m^2\,s^{-2}}$, using a test filter scale of 2Δ; (*g*) τ_{13}^{SF} contoured at intervals of $5 \times 10^{-7}\,\mathrm{m^2\,s^{-2}}$; (*h*) τ_{13}^{NL} contoured at intervals of $2 \times 10^{-5}\,\mathrm{m^2\,s^{-2}}$. In each, negative values are shaded grey and the transition from shaded to unshaded domains is the zero level.
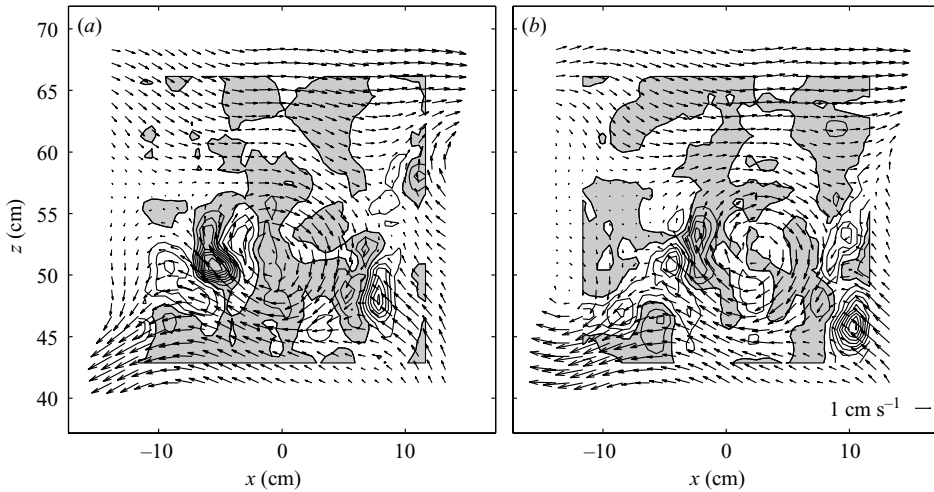
FIGURE 4. Two successive frames showing ε^{SGS} (contours) at $\Delta = 8\delta$, and the corresponding filtered velocity fluctuations (vectors). The time interval between the frames is 0.3 s and (a) is 0.3 s after figure 3. Contour intervals are 2×10^{-6} m^3 s^{-2} with negative values shaded grey. Only every second vector is plotted for clarity, and a reference vector is provided in (b).

and in apparent contradiction to predictions based on an eddy viscosity model (equation (1.8)). Regions of both positive and negative SGS dissipation are present, with peaks of opposite signs located in the vicinity of the large vortices.

The relation between the flow structures and SGS dissipation is illustrated in figure 4 using a sequence of two filtered vector maps overlaid on the ε^{SGS} distributions. It is possible to follow most of the ε^{SGS} peaks between frames, but in some cases they seem to appear or disappear. The most-likely cause of the latter is out-of-plane motion that brings different volumes of fluid into the field of view. Several negative and positive SGS dissipation peaks can be seen at the perimeter of the vortex dominating the sample area. The pattern of a positive ε^{SGS} peak ahead of large vortical structures and a negative peak trailing behind them appears repeatedly in all the boundary layer data for high and moderate turbulence levels. In flow domains without large-scale structures (not shown), the SGS dissipation appears to be weak with substantial regions of negative values.

As discussed in NS05 and mentioned earlier (see also table 1), $\langle \varepsilon^{SGS} \rangle$ almost matches $\langle \varepsilon^V \rangle$ (equation (1.7)) for the high Reynolds number series (runs A and B), but there is substantial discrepancy for the mid (runs C and D) and low (runs E and F) Reynolds number cases, where $\langle \varepsilon^{SGS} \rangle$ is one or even two orders of magnitude smaller than $\langle \varepsilon^V \rangle$. These results obviously have implications for SGS stress modelling, leading us to investigate these trends in more detail. Time series comparing the values of ε_{map}^{SGS}, calculated using a filter size of $\Delta/\delta = 8$, to ε_{map}^V of the near-bed runs (B, D and E) are presented in figure 5. In the high flow case ε_{map}^{SGS} fluctuates substantially around ε_{map}^V, but as shown in table 1, the overall average is of the same order of magnitude as $\langle \varepsilon^V \rangle$. Conversely, in the moderate mean flow case (run D, figure 5b), the SGS dissipation is consistently much lower than the viscous dissipation rate, and the average value is more than an order of magnitude lower than $\langle \varepsilon^V \rangle$. In the weak mean flow case (run F, figure 5c) but with waves, the SGS dissipation is essentially zero, except for one event that contains giant vortical structures. It is quite likely that this conspicuous 'spike' is caused by the wake of a fish or squid. Consequently, the
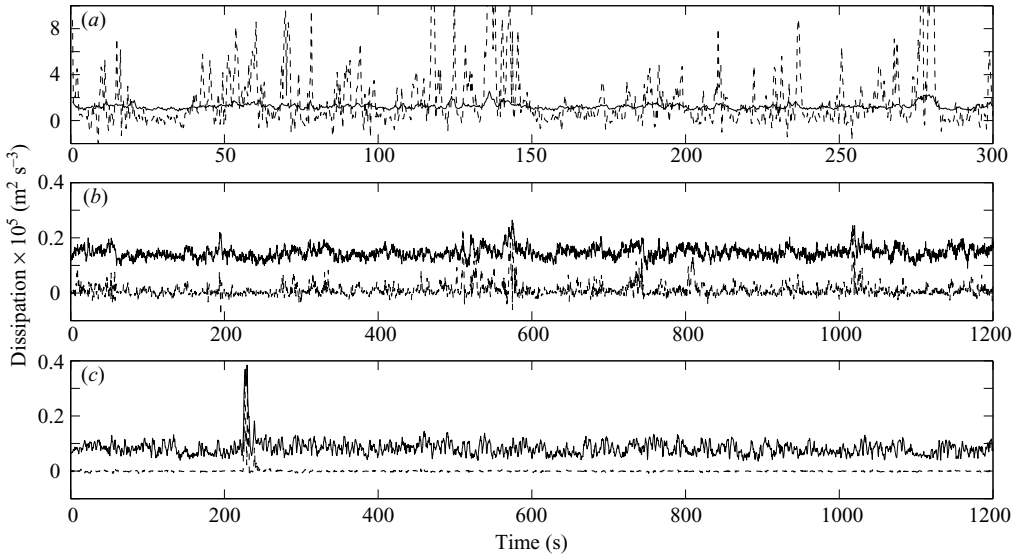
FIGURE 5. Time series comparing the sample-area mean SGS dissipation rates (ε_{map}^{SGS}) to the viscous dissipation rate (ε_{map}^{V}) for: (*a*) high flow (run B), (*b*) moderate flow (run D), and (*c*) weak flow (run F). Solid lines: ε_{map}^{V}, dashed lines: ε_{map}^{SGS} for $\Delta = 8\delta$.
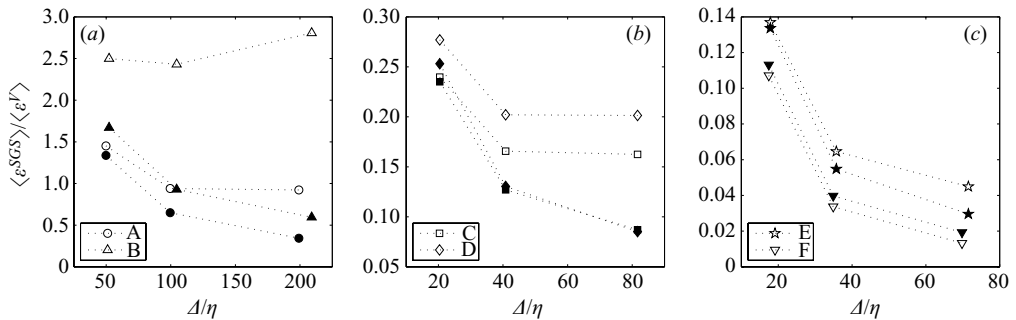
FIGURE 6. Effect of filter size (Δ) on positive and negative SGS energy fluxes. Δ is normalized by the Kolmogorov length scales (η) given in table 1. Open symbols: forwardscatter, closed symbols: backscatter. (*a*) High flow (runs A and B), (*b*) moderate flow (runs C and D), and (*c*) weak flow (runs E and F).

70 affected frames are omitted from subsequent analysis. Accordingly, the averaged value (table 1) is very close to zero and is even slightly negative. These trends agree with the DNS results of Piomelli *et al.* (1991).

The effect of filter size on positive and negative SGS energy fluxes is illustrated in figure 6. The differences between these terms, the net fluxes, are available in table 1. Note that although the primary contribution to the SGS stresses comes from the largest unresolved (filtered out) scales, at $\Delta/\delta = 4$ (leftmost point of each line), the PIV data may not resolve a sufficient range of subgrid scales, since the PIV technique itself inherently spatially filters the velocity field. However, at $\Delta/\delta = 8$ and 16, the data already cover a sufficient range of scales (Liu *et al.* 1994). In all cases the back-scatter of energy (negative flux) decreases with increasing filter size, but the transition from $\Delta/\delta = 4$ to 8 causes significantly larger decreases compared to the transition
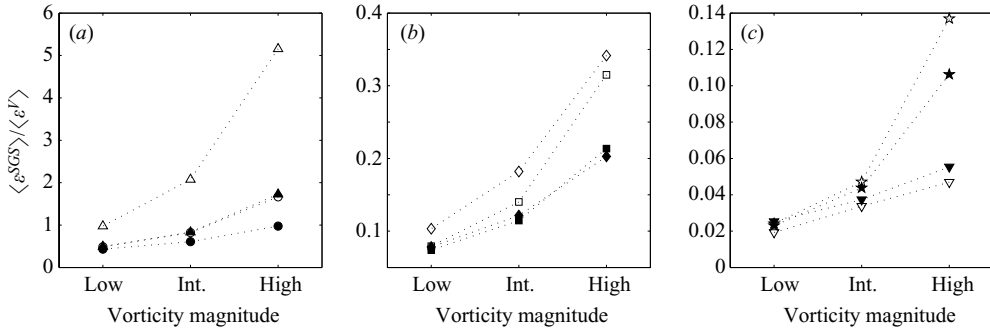
FIGURE 7. Positive and negative SGS energy fluxes, for $\Delta/\delta = 8$, conditionally sampled based on vorticity magnitude, $|\omega_y|_{map}$. High: $|\omega_y|_{map} > \langle|\omega_y|_{map}\rangle + (1/2)\ \sigma_{|\omega_y|_{map}}$; intermediate: $\langle|\omega_y|_{map}\rangle - (1/2)\ \sigma_{|\omega_y|_{map}} < |\omega_y|_{map} < \langle|\omega_y|_{map}\rangle + (1/2)\ \sigma_{|\omega_y|_{map}}$; low: $|\omega_y|_{map} < \langle|\omega_y|_{map}\rangle - (1/2)\ \sigma_{|\omega_y|_{map}}$. Open symbols: positive SGS energy flux; Closed symbols: negative SGS energy flux. Figure sections and symbol shapes as for figure 6.

from $\Delta/\delta = 8$ to 16. The forwardscatter has varying trends. In high and moderate turbulence conditions it decreases when Δ/δ increases from 4 to 8, but remains constant and even increases when Δ/δ increases from 8 to 16. In weak turbulence conditions the positive flux decreases with increasing Δ/δ. In all cases the backscatter is a substantial fraction of the forwardscatter, in agreement with laboratory data on isotropic turbulence (Liu *et al.* 1994; Tao *et al.* 2002). In the high turbulence cases, the difference is sufficient to remain close to $\langle \varepsilon^V \rangle$. In moderate and weak flow conditions both the positive and negative fluxes are smaller than $\langle \varepsilon^V \rangle$, and the difference between them reduces the net SGS dissipation to negligible levels.

In NS05 we conditionally sample the data based on the area-averaged vorticity magnitude ($|\omega_y|_{map}$) and show that the Reynolds shear stress is generated during periods of 'gusts', which are characterized by high vorticity magnitude. Here, we use the vorticity magnitude to examine whether the SGS dissipation is affected by 'gusts', as suggested by figure 4. We again opt to differentiate the flow into categories of high, intermediate and low $|\omega_y|_{map}$. The thresholds are arbitrarily set at $\langle|\omega_y|_{map}\rangle \pm (1/2)\ \sigma_{|\omega_y|_{map}}$, where $\sigma_{|\omega_y|_{map}}$ is the standard deviation of $|\omega_y|_{map}$ over the data series. The results are summarized in figure 7, showing both the positive and negative SGS energy fluxes, normalized by the viscous dissipation. Clearly, both fluxes and the difference between them increase with vorticity magnitude. For run B of the high turbulence cases, our only flows with $\varepsilon^{SGS} > \varepsilon^V$, the high SGS dissipation is clearly associated with gusts. During moderate flows $\varepsilon^{SGS} < \varepsilon^V$ even during gusts, but their ratio is only 6:1, as compared to 50:1 during quiescent periods. During low flows, ε^{SGS} remains consistently low. Therefore, in line with the underlying assumptions of homogeneity and isotropy, only flows which contain substantial numbers of vortical structures appear to have a mean SGS dissipation of a similar magnitude to the viscous dissipation.

3.2. *Effect of waves on SGS stresses and energy flux*

In applications of LES to oceanic flows, the effects of wave-induced straining on the SGS stresses and dissipation as well as on the performance of typical models are undetermined. Numerous studies have investigated the interactions between turbulence and waves, most of them focusing on phenomena occurring near the surface, and essentially all dealing with Reynolds stresses (e.g. Phillips

1959; Kitaigorodskii & Lumley 1983; Kitaigorodskii *et al.* 1983; Terray *et al.* 1996; Teixeira & Belcher 2002; Green, Medwin & Paquin 1972; Ölmez & Milgram 1992; Nepf *et al.* 1995; Thais & Magnaudet 1996). On the theoretical side, rapid distortion theory (RDT) is used by Teixeira & Belcher (2002) to show that Reynolds stresses are modified in a wave field. In the context of LES, Liu *et al.* (1999) and Chen *et al.* (2005, 2006) compare RDT predictions to laboratory measurements of SGS stresses and dissipation in rapidly strained turbulence. They show that RDT provides reasonable estimates as long as the conditions of rapid distortion are satisfied. First and foremost, for RDT to be applicable, the time scales of straining must be shorter than the eddy turnover time of the turbulence. In the context of waves and the present data, this condition implies that

$$\frac{S_{wave}u'^2}{\varepsilon} \approx \frac{u'^2\left(\dfrac{T}{\lambda}\dfrac{\partial u_{map}}{\partial t}\right)}{\varepsilon} \gg 1 \qquad (3.1)$$

where T is the period and λ is the wavelength of the surface waves. In our data $S_{wave} \approx 3 \times 10^{-4}\,\mathrm{s}^{-1}$, and $u'^2/\varepsilon = 20\,\mathrm{s}$ (e.g. for run D, NS05). Thus, $S_{wave}u'^2/\varepsilon = 6 \times 10^{-3}$, clearly not satisfying the fundamental requirement for RDT. In physical terms, this conclusion implies that wave-induced straining is much smaller than the instantaneous strain induced by the turbulence itself. It also implies that we do not have a theory that would predict the response of SGS stresses and dissipation to the wave-induced straining.

To examine the effect of waves on SGS dissipation, we use the Hilbert transform to determine the wave phase, following Hristov, Friehe & Miller (1998) and Huang *et al.* (1998). Specific procedures associated with the PIV data are discussed in Luznik (2006) and Luznik *et al.* (2007*b*) where this technique is used to examine wave-phase dependence of Reynolds stresses. We perform the analysis on flows with significant wave amplitude, i.e. runs C–F only, as runs A and B have weak wave motion relative to the mean flow and are too short (5 min) to allow reliable phase averaging. As an example, figure 8 shows a scatter plot of sample-area mean velocity components as a function of the phase of horizontal velocity (Φ^u) for run D. The zero phase is arbitrarily selected as the phase of maximum horizontal velocity, with positive phases for positive horizontal strain. The direction of wave propagation relative to the orientation of the sample area is reversed for run F due to changes in the orientation of the PIV platform. To prevent confusion, we have switched the wave-phase by $180°$ for this run to be consistent with the rest of the data. The phase lag between u_{map} and w_{map} is consistent with expectations for wave-induced flow, as discussed in detail in Luznik *et al.* (2007*b*). For conditional sampling, the data are divided evenly into 8 bins so that for runs C and D each bin contains data obtained in about 500 instantaneous realizations, and for runs E and F, about 300 realizations. However since each spatially averaged vector map provides 44×44 points for $\Delta/\delta = 8$ and 28×28 points for $\Delta/\delta = 16$, the data size in each bin of runs C and D is about 968 000 points and 392 000 points for each filter size, respectively.

Figure 9 shows the distribution of ε_{2D}^{SGS} normalized with the magnitude of their mean values for the four cases as a function of wave phase. As is evident, they all display the same trend, i.e. that the SGS dissipation peaks close to $\Phi^u = -90°$ and is significantly lower for positive phases. For run F, the SGS dissipation is negative during most of the cycle, whereas for the other cases, ε_{2D}^{SGS} is positive throughout. It would be of interest to determine the contributions to this consistent trend. Distributions of $\langle \tau_{ij}(\Phi^u) \rangle/(\varepsilon_{2D}^{SGS}\Delta)^{2/3}$, showing no significant phase dependence, are
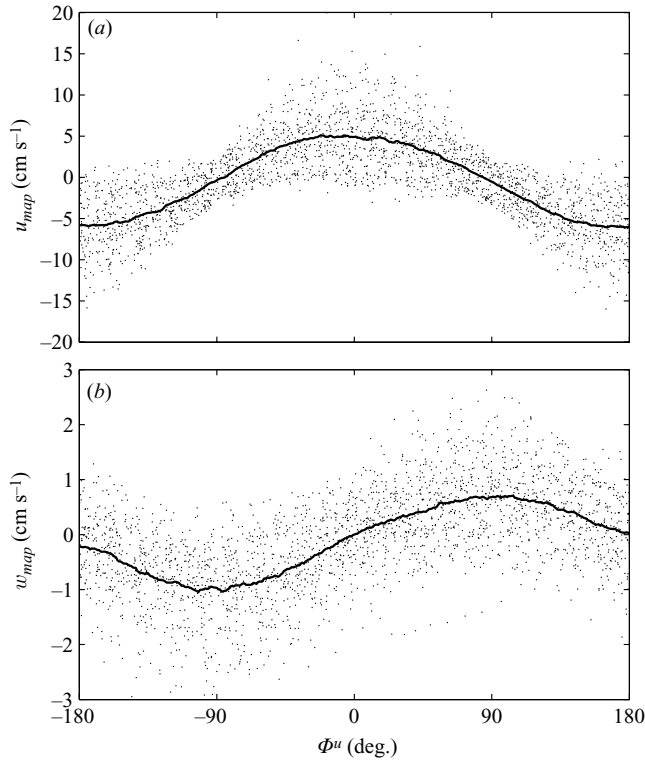
FIGURE 8. Scatter plots of (a) u_{map} and (b) w_{map} as a function of instantaneous phase for run D as determined using Hilbert transforms on a time series of spatially averaged horizontal velocity. In each, the solid line shows the conditionally sampled mean velocity based on phase.
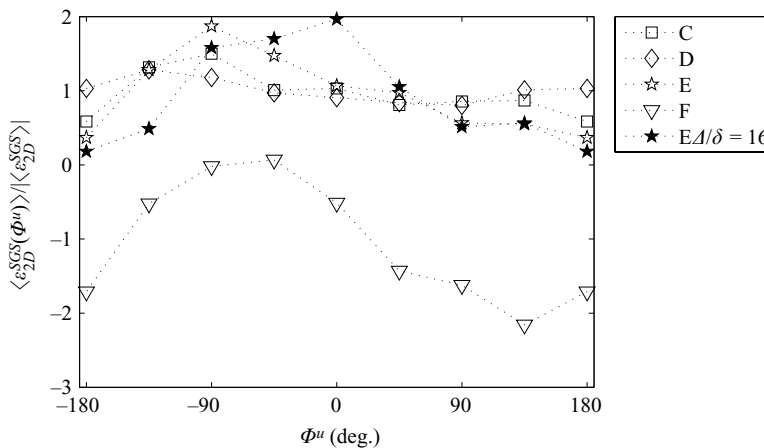

FIGURE 9. Wave phase dependence of SGS dissipation, normalized by the magnitude of the appropriate run mean SGS dissipation (see values in table 1). $\Delta/\delta = 8$ except where indicated.

presented in figure 10. As is evident, the variations of stress with phase are very small, less than 10 % for the normal stresses. These weak variations differ between runs and in general have little impact on the trends of SGS dissipation.
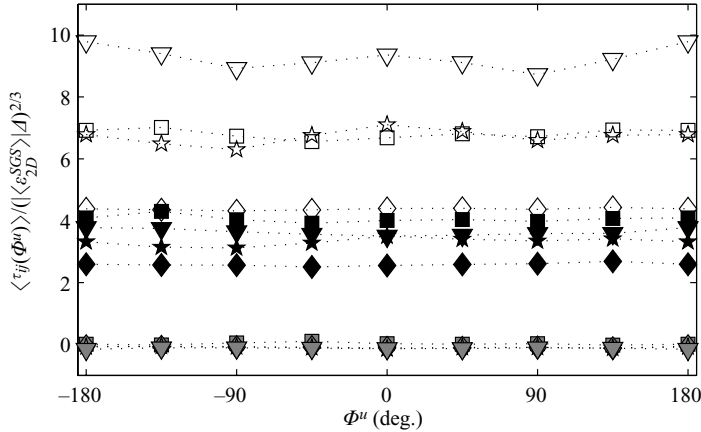
FIGURE 10. Wave phase dependence of SGS stresses normalized by $(\varepsilon_{2D}^{SGS}\Delta)^{2/3}$ for $\Delta/\delta = 8$. Symbols are the same as in figure 9; open symbols: τ_{11}; closed symbols: τ_{33}; grey symbols: τ_{13}.

In contrast to the stresses, the wave phase has a substantial effect on the distributions of $\tilde{S}_{ij}$ and $\tau_{ij}\tilde{S}_{ij}$ as shown in figure 11. We show all the cases to highlight the similarities and differences in trends. The distributions of normal strain rate components are affected by wave-induced motion, and by the local mean velocity gradients given in table 1. For all the sets, $\langle\partial u/\partial x\rangle > 0$ and $\langle\partial w/\partial z\rangle < 0$, creating constant offsets that are large for runs C and D and comparable to the wave-induced strain in runs E and F. As expected, $\tilde{S}_{11}$ peaks at $\Phi^u = 90°$, where $\tilde{S}_{33}$ is minimal, and is minimal at $\Phi^u = -90°$, where $\tilde{S}_{33}$ has its highest value. The shear strain rate is affected by the mean shear, which creates a DC offset, and presumably by slight 'wave contamination' associated with misalignment of the instrument. Their variations with phase are not consistent, and in most cases are small.

The signatures of strain variation are evident in the distributions of $-\langle\tau_{ij}\tilde{S}_{ij}(\Phi^u)\rangle$. It is easiest to start the discussion by focusing on the results of run E (figure 11f), where the mean velocity is very low. Here, $-\langle\tau_{11}\tilde{S}_{11}(\Phi^u)\rangle$ is negative for most of the cycle, where it contributes to energy backscatter, whereas $-\langle\tau_{33}\tilde{S}_{33}(\Phi^u)\rangle$ is positive over the entire cycle, i.e. on average it contributes to forwardscatter. The contribution of $-\langle\tau_{13}\tilde{S}_{13}(\Phi^u)\rangle$ is negligible. Thus, the distribution of ε_{2D}^{SGS} (figure 9) is a balance of contributions of normal components, which peak at $\Phi^u = -90°$. During positive phases, the normal components oppose each other and for negative Φ^u they are both positive. Clearly, the main contributors to the SGS energy flux are strongly affected by wave phase. The trends are similar in the other runs, although the higher DC offsets in runs C and D keep $-\langle\tau_{11}\tilde{S}_{11}(\Phi^u)\rangle$ negative and $-\langle\tau_{33}\tilde{S}_{33}(\Phi^u)\rangle$ positive over the entire cycle, with the contribution of the shear stress $-\langle\tau_{13}\tilde{S}_{13}(\Phi^u)\rangle$ adding uniform positive energy flux. The same trends persist for $\Delta/\delta = 16$, as shown in figure 11(i,j). In run F $\langle\tau_{11}\tilde{S}_{11}(\Phi^u)\rangle > \langle\tau_{33}\tilde{S}_{11}(\Phi^u)\rangle$, resulting in negative SGS dissipation for most of the cycle. Clearly, the streamwise normal strain produces energy backscatter from subgrid to resolved scales, whereas the vertical normal strain produces forward energy flux.

It is important to realize that the instantaneous magnitudes of SGS stress and filtered strain are orders of magnitude higher than the conditionally sampled mean values shown in figures 10 and 11. As an illustration, figure 12 shows joint probability density functions (PDFs) of conditionally sampled τ_{ii} and $\tilde{S}_{ii}$, along with points
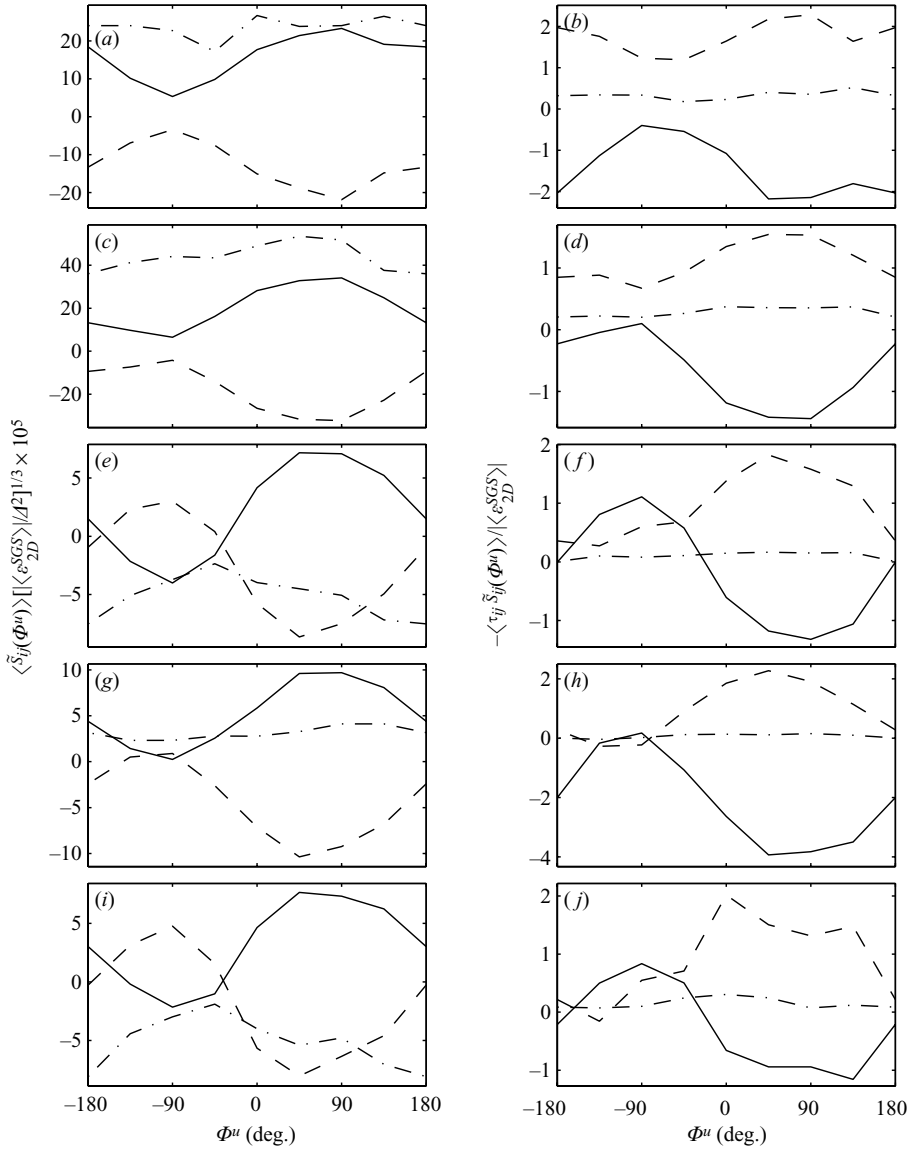
FIGURE 11. Wave phase dependence of normalized $\tilde{S}_{ij}$ (left column) and $-\tau_{ij}\tilde{S}_{ij}$ (right column) for each of the wave-influenced runs. Each row is a separate run (a, b) run C, (c, d) run D, (e, f) run E, (g, h) run F, (i, j) run G $\Delta/\delta = 16$. Solid lines: $\tilde{S}_{11}$ and $-\tau_{11}\tilde{S}_{11}$; Dashed lines: $\tilde{S}_{33}$ and $-\tau_{33}\tilde{S}_{33}$; Dash-dot lines: $\tilde{S}_{13}$ and $-\tau_{13}\tilde{S}_{13}$. $\Delta/\delta = 8$ except for the lowest row, where $\Delta/\delta = 16$.

showing their phase-average values for runs C and E. Trends for the other two runs are quite similar. We show two sample phase ranges, one with maximum $\langle \tilde{S}_{11}(\Phi^u)\rangle$ ($45° < \Phi^u < 135°$), and the other with minimum $\langle \tilde{S}_{11}(\Phi^u)\rangle$ ($-135° < \Phi^u < -45°$), the latter where ε_{2D}^{SGS} peaks. Note that the contour lines vary by factors of 10, i.e. the outer contours represent rare events. The phase-averaged values of $\langle \tilde{S}_{11}(\Phi^u)\rangle$ are very low, two orders of magnitude smaller than the peak values, and their variability with phase, shown in figure 11, is smaller than the symbol used for indicating the mean values. For each phase, the instantaneous values of $\tau_{11}\tilde{S}_{11}$ and $\tau_{33}\tilde{S}_{33}$ can be
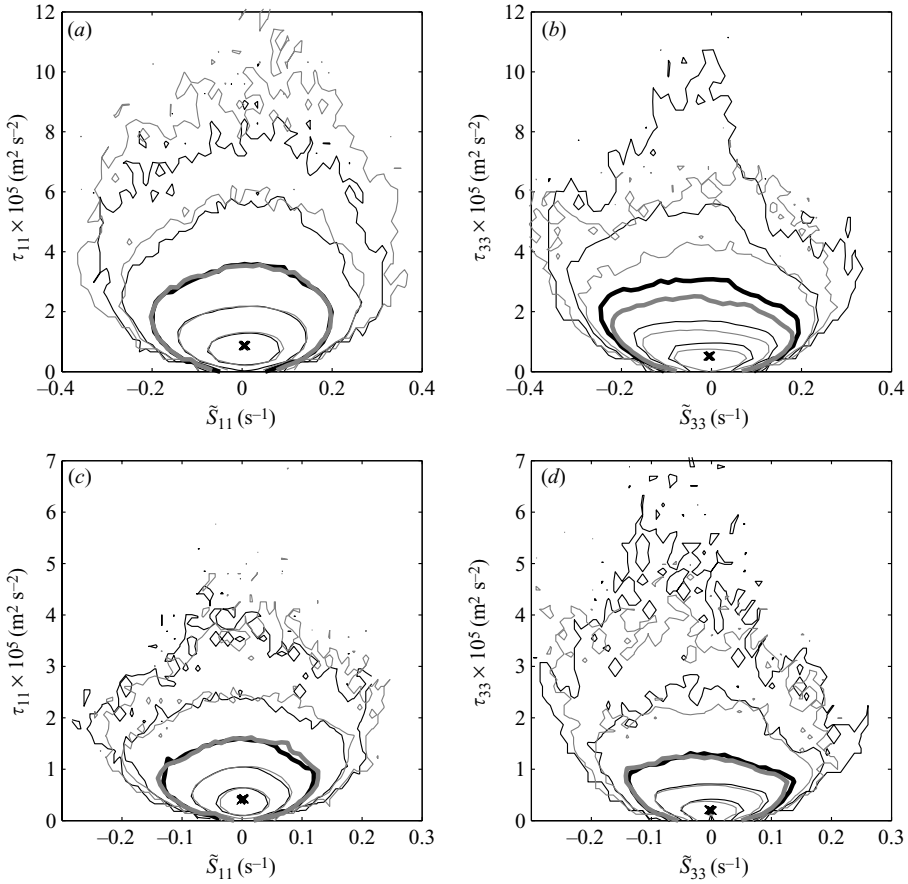
FIGURE 12. Joint PDFs of τ_{ii} and $\tilde{S}_{ii}$ conditionally sampled on wave phase for $\Delta/\delta = 8$. (a,b) run C, (c,d) run E. Black contours are for $-135° < \Phi^u < -45°$, grey contours are for $45° < \Phi^u < 135°$. Contours are at $10^{-6}, 10^{-5}, \ldots, 10^{-1}$ with the level at 10^{-4} emphasized. The crosses indicate the variation of the conditionally sampled mean values.

either positive or negative, and some are very large. The effects of wave phase are manifested by slight shifts in contours to the left or right. The distributions of τ_{11} appear to be more symmetric than the distributions of τ_{33}, especially with increasing stress magnitudes. High values of τ_{33} are clearly biased towards negative $\tilde{S}_{33}$ (forward energy scatter), whereas the peak values of τ_{11} tend slightly towards positive $\tilde{S}_{11}$ (backscatter). For the highest values of τ_{33}, the bias appears to be phase dependent, especially for run C. When we examine the instantaneous velocity distributions, it becomes evident that these extreme values are associated with frames containing large vortical structures. Since this run is recorded at an elevation of 2.5 m above the seabed, it seems unlikely that the phase dependence indicates a direct interaction with the small-scale ripples on the seabed. Clearly, the relations between SGS stress and filtered strain of horizontal and vertical components differ even for strains that are substantially larger than the wave-induced strain.

The differences between distributions of positive and negative phases, and their implications for the phase-averaged SGS dissipation are slightly confusing. Based on trends of extreme values of τ_{33}, one would expect to obtain higher $-\tau_{33}\tilde{S}_{33}(\Phi^u)$
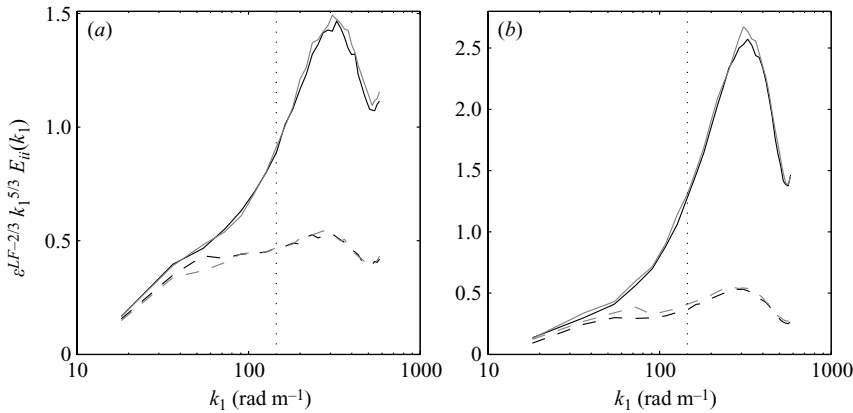
FIGURE 13. Compensated spectra ($\varepsilon^{LF\,-2/3}k_1^{5/3}E_{ii}(k_1)$) for ($a$) run C and ($b$) run E. Solid lines: $E_{11}(k_1)$; dashed lines: $E_{33}(k_1)$. Black lines: $-135° < \Phi^u < -45°$, grey lines: $45° < \Phi^u < 135°$. ε^{LF} is the spectral line-fit estimate of the dissipation taken from NS05: run C, $\varepsilon^{LF} = 7.65 \times 10^{-7}\,\mathrm{m^2\,s^{-3}}$; run E, $\varepsilon^{LF} = 1.92 \times 10^{-7}\,\mathrm{m^2\,s^{-3}}$. The vertical dotted line indicates the scale of $\Delta/\delta = 8$.

during negative phases. However, as figure 11 shows, this is clearly not the case. The reason for this apparent contradiction is the low frequency of occurrence of these extreme cases, and different trends of the low-magnitude, but orders of magnitude more frequent, events. For example, for run E and probability density of 10^{-4} or higher, the contours of negative phases are shifted slightly to the right of those at positive phases, indicating that the values of $-\tau_{33}\tilde{S}_{33}$ for $\Phi^u < 0$ are lower than those at $\Phi^u > 0$. In the case of τ_{11}, the contours of positive phases are shifted slightly to the right of those at negative phases, consistent with the values of $-\tau_{11}\tilde{S}_{11}(\Phi^u)$ being more negative when $\Phi^u > 0$. Again, the phase-dependent variations extend to levels that are much larger than the wave-induced strain.

In NS05 we show that spatial spectra of $E_{11}(k_1)$ have very large spectral 'bumps' at the transition between inertial and dissipation scales, whereas the bumps in $E_{33}(k_1)$ are much less pronounced. Here, k_1 is the wavenumber in the streamwise direction and E_{ii} is the energy density of the i velocity fluctuation component. Similar trends are observed by Luznik *et al.* (2007*a*) for higher Reynolds numbers flows at a different site. These bumps become more pronounced when the orbital wave motion is comparable with or larger than the mean flow. As examples, figure 13 shows the compensated spectra for runs C and E. As discussed in several studies (Falkovich 1994; Saddoughi & Veeravalli 1994; Champagne *et al.* 1977), and in NS05 and Luznik *et al.* (2007*a*) for coastal flows, the spectral bump is an indicator of formation of a 'bottleneck' in energy flux from large to dissipation scales. Analysis by Townsend (1961) and subsequently by Raupach, Antonia & Rajagopalan (1991) leads to the conclusion that when the spectral slope decreases to k^{-1}, the cascading process of energy from large to small scales ceases. The large bumps in E_{11} indicate there is less flux in the horizontal component of the turbulent kinetic energy, compared to the vertical component. Furthermore, since the slope of $E_{11}(k_1)$ before the peak is about k^{-1} or even larger (Luznik *et al.* 2007*a*), energy cascading to small scales at least ceases at this range of wavenumbers. As discussed before, the values of $-\tau_{ij}\tilde{S}_{ij}$ are direct measures of energy flux from resolved to subgrid scales at the filter scale. Our data show that $-\langle\tau_{11}\tilde{S}_{11}(\Phi^u)\rangle$ is mostly negative, indicating backscatter of energy, whereas

$-\langle \tau_{33} \tilde{S}_{33}(\Phi^u) \rangle$ is positive, i.e. forwardscatter persists at all phases. The filter scale falls to the left of the peak in the spectral bumps, as indicated by the dotted lines in figure 13. Thus, the present analysis of SGS energy fluxes suggests that the spectral bump, i.e. the reduction and even stoppage of energy cascading in the horizontal component, is caused at least in part by the combined effects of straining by the mean flow and wave-induced motion. Conversely, the spectral bumps in $E_{33}(k_1)$ are much smaller, consistent with the energy flux being predominantly positive. This assertion is further supported by trends of $E_{11}(k_1)$ with wave phase. As figure 13 shows, the peaks of the bumps in $E_{11}(k_1)$ are marginally higher when $\Phi^u > 0$ ($45° < \Phi^u < 135°$) i.e. when the backscatter is higher, than their values when $\Phi^u < 0$, i.e. when the backscatter is small.

Our postulate that the combined effect of the straining by the mean flow and wave-induced motion enhances the spectral bumps of $E_{11}(k_1)$ obviously requires a more complete formal proof. This would involve decomposition of the terms contributing to the SGS energy fluxes to contributions of mean flow, wave-induced motion and turbulence, similar to the analysis performed by Liu *et al.* (1999) and Chen *et al.* (2006) for rapidly strained flows. We are unable to perform this decomposition with the present data since we cannot completely separate wave motion and turbulence. However there is clear consistency between the fact that $E_{11}(k_1)$ has large bumps, larger than any previously published results, and that these also increase in accordance with wave-phase trends of energy backscatter.

3.3. *A priori test results*

The term '*a priori* testing' of stress models has been coined by Piomelli *et al.* (1988) to describe a direct comparison between measured and modelled SGS stresses, as opposed to comparisons based on the results of simulations. Figure 3(*e–h*) shows the instantaneous distributions of the Smagorinsky model prediction (τ_{13}^S), the dynamic model prediction (τ_{13}^D), the prediction of the structure function model (τ_{13}^{SF}) and the prediction of the nonlinear model (τ_{13}^{NL}), for the velocity field of figure 2(*b*) and the measured τ_{13}^{SGS} of figure 3(*c*). Consistent with Liu *et al.* (1994), the distribution of predictions of the nonlinear model bear considerable resemblance to the measured stress, although the predicted magnitudes of the peaks are substantially larger than the measured values. The Smagorinsky model, on the other hand, looks significantly different, in accordance with the distribution of the filtered strain (figure 3*d*). As would be expected, both the dynamic and structure function model predictions also show broad similarities with the predictions of the Smagorinsky model, although with differences in magnitude and small-scale structure. In particular, the dynamic model generates much greater variability over much smaller scales.

3.3.1. *Correlation coefficients*

Following Liu *et al.* (1994), one may start the analysis by examining the correlation coefficients between the measured and modelled stresses,

$$\rho\left(\tau_{ij}^m, \tau_{ij}^{SGS}\right) = \frac{\langle \tau_{ij}^m \tau_{ij}^{SGS} \rangle - \langle \tau_{ij}^m \rangle \langle \tau_{ij}^{SGS} \rangle}{\left[\left(\langle (\tau_{ij}^m)^2 \rangle - \langle \tau_{ij}^m \rangle^2 \right) \left(\langle (\tau_{ij}^{SGS})^2 \rangle - \langle \tau_{ij}^{SGS} \rangle^2 \right) \right]^{1/2}} \tag{3.2}$$

where τ_{ij}^m is τ_{ij}^S, τ_{ij}^D, τ_{ij}^{SF} or τ_{ij}^{NL}. The results are presented in table 2. Consistent with previously observed trends, the correlation coefficients of the nonlinear model are substantially higher than those of the Smagorinsky model (see discussion in Meneveau & Katz 2000). For the nonlinear models, the correlation coefficients tend to decrease with decreasing filter size and Re_λ. These trends, but with more variability

Run	A	B	C	D	E	F	Lab
$\rho(\tau_{13}^{S}, \tau_{13}^{SGS})\ (\Delta/\delta = 4)$	0.060	0.171	0.045	0.062	0.024	0.006	0.220
$\rho(\tau_{13}^{S}, \tau_{13}^{SGS})\ (\Delta/\delta = 8)$	0.178	0.338	0.162	0.179	0.077	0.045	0.264
$\rho(\tau_{13}^{S}, \tau_{13}^{SGS})\ (\Delta/\delta = 16)$	0.348	0.437	0.298	0.249	0.158	0.127	0.263
$\rho(\tau_{13}^{D}, \tau_{13}^{SGS})\ (\Delta/\delta = 8)$ All data	0.064	0.188	0.035	0.076	0.039	0.012	0.058
Threshold: $\langle M_{ij}M_{ij}\rangle \times 10^{8}\ (m^4 s^{-4})$	48	207	0.31	0.33	0.019	0.003	3400
% data above threshold	13.3	16.8	13.1	13.3	13.7	20.6	14.2
$\rho(\tau_{13}^{D}, \tau_{13}^{SGS})\ (\Delta/\delta = 8)$ above threshold	0.301	0.400	0.238	0.294	0.086	0.055	0.209
% data above 2× threshold	8.1	10.2	7.7	7.6	8.6	12.3	8.7
$\rho(\tau_{13}^{D}, \tau_{13}^{SGS})\ (\Delta/\delta = 8)$ above 2× threshold	0.358	0.417	0.261	0.315	0.087	0.111	0.195
$\rho(\tau_{13}^{SF}, \tau_{13}^{SGS})\ (\Delta/\delta = 8)$	0.168	0.327	0.148	0.161	0.073	0.043	0.233
$\rho(\tau_{13}^{NL}, \tau_{13}^{SGS})\ (\Delta/\delta = 4)$	0.598	0.698	0.588	0.613	0.520	0.482	0.790
$\rho(\tau_{13}^{NL}, \tau_{13}^{SGS})\ (\Delta/\delta = 8)$	0.675	0.772	0.721	0.738	0.625	0.404	0.788
$\rho(\tau_{13}^{NL}, \tau_{13}^{SGS})\ (\Delta/\delta = 16)$	0.804	0.821	0.817	0.785	0.733	0.691	0.782

TABLE 2. Correlation coefficients between modelled and measured SGS shear stresses. τ_{13}^{D} is calculated using a test filter scale of 2Δ.

and lower values, apply also to the Smagorinsky model. Overall, these results suggest that the nonlinear model would make the best choice for modelling the SGS stresses in the present ocean flows. However, as will be discussed shortly, the low SGS dissipation of the ocean data at low Re_λ makes application of this model problematic.

In spite of the poor correlation of the Smagorinsky model it has been popular since it 'behaves' well in LES, while generating the appropriate level of positive SGS dissipation. In figure 14 we use a joint PDF of ε^{SGS} (normalized by $\langle\varepsilon^{SGS}\rangle$) and $|\tilde{S}|$ (normalized by its r.m.s. value, $\sigma_{|\tilde{S}|}$) to explore the relationship between SGS dissipation and strain magnitude for runs B, D and F. In all cases, the iso-probability lines expand both in the positive and negative directions with increasing $|\tilde{S}|$. However, in high and moderate turbulence level flows the expansion is higher in the positive direction, consistent with Tao *et al.* (2002), whereas in the weak flow case, the expansion deviates slightly in the negative direction (recall that the values are very low). Since according to the Smagorinsky model ε^{SGS} is proportional to $|\tilde{S}|^3$, figures 14(*a*) and 14(*b*) also compare the conditionally sampled SGS dissipation (based on strain magnitude) to best-fitted cubic polynomials. The results appear to be quite good in high and moderate flow conditions, but in the low flow conditions the negative trend of the conditionally sampled ε^{SGS} with increasing $|\tilde{S}|$ cannot be fitted. A cubic relationship is not consistent with the implied proportionality between ε^{SGS} and $|\tilde{S}|^2$ of the structure function model.

The correlation coefficients between the measured stress and those predicted using a locally evaluated dynamic model are also presented in table 2. These results require care in their interpretation as will be explained, but without thresholding they have very low values. With thresholding based on $M_{ij}M_{ij}$ values, they show a distinct improvement over the static Smagorinsky and structure function models, while still not reaching the levels of the nonlinear model. As shown in figure 3(*f*) and reported in Liu, Meneveau & Katz (1995), without any averaging, the dynamic model yields a highly variable eddy viscosity field. Liu *et al.* (1995) show that small values of $M_{ij}M_{ij}$, which are close to zero, substantially bias the coefficient values. They suggest that these small values should be discarded when evaluating trends of correlations because
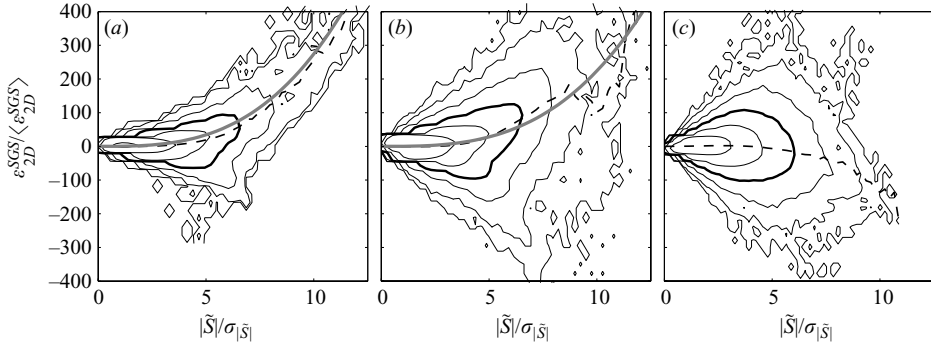
FIGURE 14. Joint PDFs of SGS dissipation rate with the strain-rate magnitude for $\Delta/\delta = 8$. The values of ε^{SGS} are normalized by $\langle \varepsilon^{SGS} \rangle$, given in table 1, and $|\tilde{S}|$ is normalized by $\sigma_{|\tilde{S}|}$. (a) run B, $\sigma_{|\tilde{S}|} = 0.246\,\mathrm{s}^{-1}$; (b) run D, $\sigma_{|\tilde{S}|} = 0.072\,\mathrm{s}^{-1}$; (c) run F, $\sigma_{|\tilde{S}|} = 0.025\,\mathrm{s}^{-1}$. Contour levels are at $10^{-7}, 10^{-6}, \ldots, 10^{-1}$, with the level at 10^{-4} emphasized. The dashed line shows the normalized, conditionally sampled (based on $|\tilde{S}|/\sigma_{|\tilde{S}|}$) mean SGS dissipation. The grey solid line in (a) is $0.27(|\tilde{S}|/\sigma_{|\tilde{S}|})^3$ and in (b), $0.22(|\tilde{S}|/\sigma_{|\tilde{S}|})^3$.

Run	A	B	C	D	E	F	Lab
c_S ($\Delta/\delta = 4$)	0.02	0.13	0.04	0.07	0.08	–	0.19
c_S ($\Delta/\delta = 8$)	0.10	0.19	0.10	0.14	0.14	–	0.23
c_S ($\Delta/\delta = 16$)	0.19	0.23	0.13	0.17	0.16	–	0.26
c_D ($\Delta/\delta = 8$)	0.24	0.21	0.17	0.20	0.19	0.06	0.26
C_{SF} ($\Delta/\delta = 8$)	0.33	0.78	0.23	0.37	0.34	−1.04	1.15
$K_m \times 10^5$ ($\Delta/\delta = 8$)	6.16	8.27	1.17	1.24	0.58	0.47	3.58
C_{NL} ($\Delta/\delta = 8$)	0.08	0.19	0.09	0.12	0.14	−0.48	0.26

TABLE 3. 'Global' model coefficients.

of the experimental error associated with individual measurements. Repeating our analysis using increasing threshold levels of $M_{ij}M_{ij}$ indeed shows a marked increase in correlation values, particularly when the threshold levels exceed $\langle M_{ij}M_{ij} \rangle$ representing $13\% - 20\%$ of the data.

3.3.2. *Measured model coefficients*

The measured (static) Smagorinsky model coefficients (equation (1.13)) are presented in table 3. They increase with filter size, more as Δ/δ increases from 4 to 8 and to a lesser extent when Δ/δ increases from 8 to 16. Since, as noted before, the values at $\Delta/\delta = 4$ may be affected by an insufficient range of subgrid scales, we focus on trends of the larger two filters. For $\Delta/\delta = 8$ and 16, the coefficients of the laboratory reference data and those of run B (0.186–0.226) are close to, but larger than, theoretically obtained values for isotropic turbulence (0.16, Lilly 1967). The results of run A are lower and increase more sharply with filter size, from 0.10 at $\Delta/\delta = 8$ to 0.19 at $\Delta/\delta = 16$. Thus, the 5–6 times decrease in mean SGS dissipation between runs B and A (table 1) is accompanied by a similar but slightly lower decrease in the magnitudes of $|\tilde{S}|^3$. As Re_λ decreases to moderate levels, the values

of c_S decrease further, to 0.10–0.13 and 0.14–0.17 for run C and D, respectively. For one of the weak flow conditions we obtain similar values, in the 0.14–0.16 range. The results for run F are not presented since the coefficients are negative due to the very low but negative mean SGS dissipation. Therefore, the general trend is a slight decrease in the Smagorinsky coefficient with decreasing turbulence level. As discussed in NS05, and shown in figure 13, for all the present data, the turbulence is nearly isotropic at low wavenumbers but becomes increasingly anisotropic as the spectral bumps form. Thus, the level of anisotropy at the filter scale decreases with increasing Δ/δ. Consistent with the conclusions of Horiuti (1993), our results suggest that the Smagorinsky coefficient decreases with increasing levels of anisotropy. However, unlike trends reported by Porte-Agel *et al.* (2000), the coefficients of runs B and D are higher than those of runs A and C respectively, in spite of being measured closer to the bottom where the mean shear rates are higher.

The values of the dynamic model coefficients (c_D) calculated using 'global' ensemble averages, and shown in table 3, are mostly higher than the static coefficients, but they follow similar trends. The values of c_D for $\Delta/\delta = 8$ are consistently closer to those of c_S for $\alpha\Delta$ ($\Delta/\delta = 16$), the scale of the larger filter used for calculating them. Such trends have been observed before, leading Porte-Agel *et al.* (2000) to introduce a scale-dependent dynamic model, where the scale-dependence correction factor is calculated using test filters at $\alpha\Delta$ and at $\alpha^2\Delta$. Unfortunately, the finite extent of our sample area prevents us from testing this model since it requires filtering and calculating derivatives at a scale of 4Δ.

The behaviour of the structure function model can be examined by calculating equivalent 'global model coefficients', $C_{SF} = \langle\varepsilon^{SGS}\rangle/\langle\varepsilon^{SF}\rangle$, where $\varepsilon^{SF} = -\tau_{ij}^{SF}\tilde{S}_{ij}$ is the SGS dissipation estimated from the modelled stresses. The results are shown in table 3. For the isotropic turbulence laboratory data, the structure function model underestimates the mean SGS dissipation rate by only 15%. For run B, the near-bed, high-Re_λ and least anisotropic set, the model overestimates the SGS dissipation by 28%. However, away from the seabed, as well as at moderate and low Re_λ, the structure function model consistently overestimates the SGS dissipation rate by $\sim 300\%$–400%. These latter trends are consistent with previous observations (Piomelli 1999).

The coefficients of the nonlinear model fluctuate between 0.08 and 0.19 for runs A–E, all being smaller than the laboratory results. They seem to have higher values with increasing mean shear, but there is no clear trend with Re_λ. The low turbulence levels of run F lead to meaningless results.

Before concluding this section and in view of the effect of waves on ε^{SGS}, we examine the effects of wave phase on the model coefficients discussed within this section. The results for runs C, D and E are presented in figure 15. The distributions of c_S show a persistent increase at negative phases, indicating that the variations of energy flux with phase are higher than those of $|\tilde{S}|^3$. The origins of these trends can be identified in figure 11. For example, for run E, the normal filtered strain components oscillate between positive and negative values, whereas the corresponding SGS dissipation terms are all positive when $\Phi^u < 0$. Note that the Smagorinsky model does not allow energy backscatter, that is the modelled $-\tau_{11}^S\tilde{S}_{11}$ will be positive, unlike the measured trends. Thus, if we examine its performance based on individual components, the modelled streamwise contribution to the SGS dissipation will have the wrong sign.

The nonlinear and structure function model coefficients display variations with phase that are similar to those of c_S. Even the difference between trends of different runs persist. However, the extent of variations, e.g. the ratio between maximum and
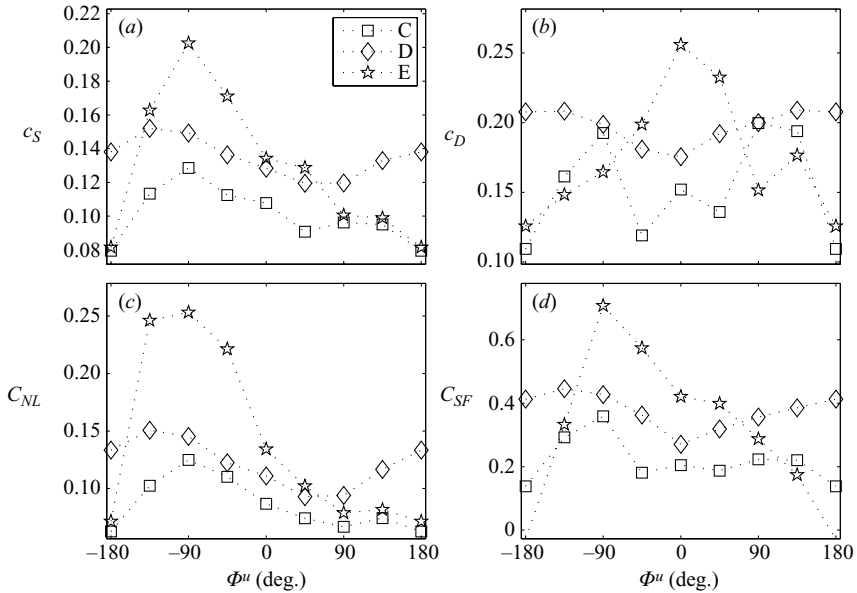
FIGURE 15. Model coefficients conditionally sampled based on wave phase. (*a*) c_S, (*b*) c_D, (*c*) C_{NL}, (*d*) C_{SF}. Symbols are as for figure 9 and $\Delta/\delta = 8$. Run F not shown.

minimum values, differ. The changes in C_{NL} are about twice as high as those of c_S, and the changes in C_{SF} are even higher. These persistent trends are all a result of the inability of the modelled SGS dissipation to fully reproduce the measured phase-dependent changes. The static Smagorinsky model reproduces some of the trend, and as a result the model coefficient, e.g. for run D or E, change to a lesser extent than ε^{SGS}. The nonlinear and structure function models are less successful, resulting in higher fluctuations in the coefficients.

Trends of the dynamic coefficient for runs C and D are similar to those of the static coefficient although they are more jittery, in part due to the smaller sample size resulting from the second filtering process. For run E, the peak of c_D shifts to a different phase, but the minimum is still around $\pm 180°$.

4. Concluding remarks

Six data sets obtained using PIV measurements in the bottom boundary layer of the coastal ocean (and one reference laboratory set) are used to examine the characteristics of SGS stresses and dissipation as well as the performance of several SGS stress models. The ocean data sets are selected to represent conditions of high, moderate and low Taylor-microscale turbulent Reynolds numbers, close to the seabed (in the 20–70 cm range) and far from it (2.5 m).

As noted by Nimmo Smith *et al.* (2005), in the high-Re_λ conditions, the SGS dissipation is close in magnitude to the viscous dissipation, consistent with the laboratory data. However, in the moderate and weak flows, the SGS dissipation is much smaller, by more than an order of magnitude, than the viscous dissipation rate. Here we show that while localized peaks in both positive and negative dissipation are associated with vortical structures within the flow, the levels of positive SGS dissipation increase more than the negative SGS dissipation during periods of high vorticity magnitude. This relative increase in positive SGS dissipation allows average

SGS dissipation values to approach the viscous dissipation. Therefore, moderate and low Reynolds number flows, that contain few vortical structures, do not allow the underlying assumptions that equate ε^{SGS} to ε^V to be made.

To examine the effects of waves on turbulence, it would have been insightful to examine the contributions of mean flow, waves and large-scale turbulence separately. However, to perform such an analysis, one has to decompose the unsteady component of the flow to contributions of waves and turbulence. Since the amplitude and period of waves in the ocean vary constantly, we cannot decompose these two unsteady contributors. However, the Hilbert transform enables us to estimate the wave phase, and use conditional sampling to examine the variations of different variables with this phase. Conditional sampling of SGS dissipation and filtered strain provide clear evidence that the SGS energy fluxes vary significantly with wave phase. The same trends persist in all the coastal flow measurements, with or without mean velocity. The magnitude of ε^{SGS} peaks when the horizontal component of wave-induced velocity accelerates (when the vertical component is minimal), and is low when the horizontal wave velocity decelerates. Since ε^{SGS} represents the energy flux from resolved to subgrid scales, our data demonstrate that large scale but weak wave-induced straining directly affects the energy cascading process at small scales. This effect cannot be modelled by rapid distortion theory since the straining time scale is much larger than the eddy turnover time. Indeed, the turbulence-induced strain extends to values that are orders of magnitude higher than the wave strain. Phase-dependent effects can be observed over the entire joint PDF of SGS stress and filtered strain, including values that are much larger than the wave contribution. These effects are observed even at the higher sampling elevations of 2.5 m, making direct flow interaction with the small seabed ripples (< 10 cm height) unlikely.

Furthermore, we show that the contribution of the streamwise velocity component to ε^{SGS} is negative, i.e. it causes energy backscatter from subgrid to resolved scales, especially when combined with effects of local mean strain. This backscatter may explain the formation of large bumps in the energy spectra of the horizontal velocity component at the transition from inertial to dissipation scales. The contribution of the vertical velocity component is positive. The effect of shear on SGS energy flux is small but positive, presumably since the coastal flows analysed here are moderate to weak (but typical). We will repeat the analysis using higher Reynolds number data in the future.

Four SGS stress models are examined. The correlations between modelled and predicted stresses follow expected trends (Meneveau & Katz 2000): the Smagorinsky model with constant coefficient and the structure function model display poor correlations, whereas the nonlinear model achieves the highest correlation. The correlation coefficients of the dynamic model improve with increasing filtered strain magnitude. The ability of these models to reproduce instantaneous distributions of SGS stresses is consistent with these conclusions. The measured Smagorinsky model coefficients increase with filter scale. During moderate and weak flow conditions, these coefficients are distinctly lower than those measured for high turbulence in the laboratory and ocean (see table 3). The dynamic model coefficients are consistently higher than the static values, and appear to be comparable to results obtained for larger filter scales, consistent with the observations that have led to the development of the scale-dependent dynamic model (Porte-Agel *et al.* 2000). For all the ocean data, the structure function model is too dissipative. The ratio between measured and modelled SGS dissipation ranges between 0.23 and 0.78, decreasing with increasing distance from the bottom and as the Reynolds number decreases. In contrast, the

structure function model very slightly underestimates the SGS dissipation in the laboratory reference data.

The variations of ε^{SGS} with wave phase also affect the values of model coefficients. For models whose coefficients are determined based on ε^{SGS}, since the model variables do not vary to the same extent as the SGS dissipation, the model coefficients become phase dependent. The extent of variations differs, but trends are similar. The variations of the static Smagorinsky coefficient with phase seem to be lower than those of the dynamic Smagorinsky and nonlinear models, indicating that its variables ($\varepsilon^{S} \propto |\tilde{S}|^3$) follow the measured trends better than those of the other models. However, since the Smagorinsky model does not allow for energy backscatter, it inherently cannot predict the negative contribution of the streamwise component measured here. The conditionally sampled values of dissipation predicted by the structure function model also do not follow the measured variations with phase.

Finally, a word of caution. While the observed trends are repeatable and statistically robust, we are unable to identify or explain the exact mechanisms causing them. Future studies, either in controlled laboratory conditions or at other field sites with different wave, current and bottom characteristics, are therefore essential for elucidating the effect of large scale but weak wave-induced straining on the energy cascading processes at small scales.

REFERENCES

BERTUCCIOLI, L., ROTH, G. I., KATZ, J. & OSBORN, T. R. 1999 A submersible particle image velocimetry system for turbulence measurements in the bottom boundary layer. *J. Atmos. Oceanic Technol.* **16**, 1635–1646.

BORUE, V. & ORSZAG, S. A. 1998 Local energy flux and subgrid-scale statistics in three-dimensional turbulence. *J. Fluid Mech.* **366**, 1–31.

CHAMPAGNE, F. H., FRIEHE, C. A., LA RUE, J. C. & WYNGAARD, J. C. 1977 Flux measurements, flux estimation techniques and fine scale turbulence measurements in the surface layer over land. *J. Atmos. Sci.* **34**, 515–530.

CHEN, J., KATZ, J. & MENEVEAU, C. 2005 Implication of mismatch between stress and strain-rate in turbulence subjected to rapid straining and destraining on dynamic LES models. *Trans. ASME: J. Fluids Engng* **127**, 840–850.

CHEN, J., MENEVEAU, C. & KATZ, J. 2006 Scale interactions of turbulence subjected to a straining–relaxation–detraining cycle. *J. Fluid Mech.* **562**, 123–150.

DEARDORFF, J. W. 1980 Stratocumulus-capped mixed layers derived from a three-dimensional model. *Boundary Layer Met.* **18**, 495–527.

DENBO, D. W. & SKYLLINGSTAD, E. D. 1996 An ocean large-eddy simulation model with application to deep convection in the Greenland Sea. *J. Geophys. Res.* **101** (C1), 1095–1110.

DORON, P., BERTUCCIOLI, L., KATZ, J. & OSBORN, T. R. 2001 Turbulence characteristics and dissipation estimates in the coastal ocean bottom boundary layer from PIV data. *J. Phys. Oceanogr.* **31**, 2108–2134.

FALKOVICH, G. 1994 Bottleneck phenomenon in developed turbulence. *Phys. Fluids* **6**, 1411–1414.

FRIEDMAN, P. D. & KATZ, J. 2002 Mean rise-rate of droplets in isotropic turbulence. *Phys. Fluids* **6**, 1411–1414.

GERMANO, M., PIOMELLI, U., MOIN, P. & CABOT, W. H. 1991 A dynamic subgrid-scale eddy viscosity model. *Phys. Fluids* A **3**, 1760.

GREEN, T., MEDWIN, H. & PAQUIN, J. E. 1972 Measurements of surface wave decay due to underwater turbulence. *Nature* **237**, 115–117.

HORIUTI, K. 1993 A proper velocity scale for modelling subgrid-scale eddy viscosities in large-eddy simulation. *Phys. Fluids* A **5**, 146–157.

HRISTOV, T., FRIEHE, C. & MILLER, S. 1998 Wave-coherent fields in air flow over ocean waves: identification of cooperative behavior buried in turbulence. *Phys. Rev. Lett.* **81**, 5245–5248.

HUANG, N. E., SHEN, Z., LONG, S. R., WU, M. C., SHIH, H. H., ZHENG, Q., YEN, N., TUNG, C. C. & LIU, H. H. 1998 The empirical mode decomposition and the Hilbert spectrum for nonlinear and non-stationary time series analysis. *Proc. R. Soc. Lond.* A **454**, 903–995.

KITAIGORODSKII, S. A., DONELAN, M. A., LUMLEY, J. L. & TERRAY, E. A. 1983 Wave-turbulence interactions in the upper ocea. Part II: Statistical characteristics of wave and turbulent components of the random velocity field in the marine surface layer. *J. Phys. Oceanogr.* **13**, 1988–1999.

KITAIGORODSKII, S. A. & LUMLEY, J. L. 1983 Wave-turbulence interactions in the upper ocean. Part I: The energy balance on the interacting fields of surface wind waves and wind-induced three-dimensional turbulence. *J. Phys. Oceanogr.* **13**, 1977–1987.

LEONARD, A. 1974 Energy cascade in large-eddy simulations of turbulent fluid flows. *Adv. Geophys.* **18**, 237–248.

LESIEUR, M. & METAIS, O. 1996 New trends in large-eddy simulations of turbulence. *Annu. Rev. Fluid Mech.* **28**, 45–82.

LI, M., SANFORD, L. & CHAO, S. Y. 2005 Effects of time dependence in unstratified tidal boundary layers: results from large eddy simulations. *Estuarine, Coastal Shelf Sci.* **62**, 193–204.

LILLY, D. K. 1967 The representation of small-scale turbulence in numerical simulations. In *Proc. IBM Scientific Computing Symposium on Environmental Sciences*, pp. 195–209. IBM form no. 320-1951, White Plains, New York.

LILLY, D. K. 1992 A proposed modification of the Germano subgrid-scale closure method. *Phys. Fluids* A **4**, 633–635.

LIU, S., KATZ, J. & MENEVEAU, C. 1999 Evolution and modeling of subgrid scales during rapid straining of turbulence. *J. Fluid Mech.* **387**, 281–320.

LIU, S., MENEVEAU, C. & KATZ, J. 1994 On the properties of similarity subgrid-scale models as deduced from measurements in a turbulent jet. *J. Fluid Mech.* **275**, 83–119.

LIU, S., MENEVEAU, C. & KATZ, J. 1995 Experimental study of similarity subgrid-scale models of turbulence in the far-field of a jet. *Appl. Sci. Res.* **54**, 177–190.

LUZNIK, L. 2006 Turbulence characteristics of a tidally driven bottom boundary layer of the coastal ocean. PhD thesis, The Johns Hopkins University.

LUZNIK, L., GURKA, R., NIMMO SMITH, W. A. M., ZHU, W., KATZ, J. & OSBORN, T. R. 2007*a* Distribution of energy spectra, Reynolds stresses, turbulence production and dissipation in a tidally driven bottom boundary layer. *J. Phys. Oceanogr.* (in press).

LUZNIK, L., NIMMO SMITH, W. A. M., OSBORN, T. R., & KATZ, J. 2007*b* Turbulence and waves in the bottom boundary layer of the coastal ocean. *J. Phys. Oceanogr.* (submitted).

MASON, P. J. 1989 Large-eddy simulation of the convective atmospheric boundary layer. *J. Atmos. Sci.* **46**, 1492–1516.

MENEVEAU, C. & KATZ, J. 1999 Dynamic testing of subgrid models in large eddy simulation based on the Germano identity. *Phys. Fluids* **11**, 245–247.

MENEVEAU, C. & KATZ, J. 2000 Scale-invariance and turbulence models for large-eddy simulation. *Annu. Rev. Fluid Mech.* **32**, 1–32.

METAIS, O. & LESIEUR, M. 1992 Spectral large-eddy simulation of isotropic and stably stratified turbulence. *J. Fluid Mech.* **239**, 157–194.

MIN, H. S. & NOH, Y. 2004 Influence of the surface heating on Langmuir circulation. *J. Phys. Oceanogr.* **34**, 2630–2641.

MOIN, P. & KIM, J. 1982 Numerical investigation of turbulent channel flow. *J. Fluid Mech.* **118**, 341–377.

NEPF, H. M., COWEN, E. A., KIMMEL, S. J. & MONISMITH, S. G. 1995 Longitudinal vortices beneath breaking waves. *J. Geophys. Res.* **100**, 16211–16221.

NIMMO SMITH, W. A. M., ATSAVAPRANEE, P., KATZ, J. & OSBORN, T. R. 2002 PIV measurements in the bottom boundary layer of the coastal ocean. *Exps. Fluids* **33**, 962–971.

Nimmo Smith, W. A. M., Katz, J. & Osborn, T. R. 2005 On the structure of turbulence in the bottom boundary layer of the coastal ocean. *J. Phys. Oceanogr.* **35**, 72–93 (referred to herein as NS05).

Nimmo Smith, W. A. M., Osborn, T. R. & Katz, J. 2004 PIV measurements in the bottom boundary layer of the coastal ocean. In *PIV and Water Waves* (ed. J. Grue, P. L.-F. Liu & G. K. Pedersen). Advances in Coastal and Ocean Engineering, vol. 9, chap. 2, pp. 51–79. World Scientific.

Noh, Y., Min, H. S. & Raasch, S. 2004 Large eddy simulation of the ocean mixed layer: the effects of wave breaking and Langmuir circulation. *J. Phys. Oceanogr.* **34**, 720–735.

Ölmez, H. S. & Milgram, J. H. 1992 An experimental study of attenuation of short water waves by turbulence. *J. Fluid Mech.* **239**, 133–156.

Phillips, O. M. 1959 The scattering of gravity waves by turbulence. *J. Fluid Mech.* **5**, 177–192.

Piomelli, U. 1999 Large-eddy simulation: achievements and challenges. *Prog. Aerospace Sci.* **35**, 335–362.

Piomelli, U., Cabot, W. H., Moin, P. & Lee, S. 1991 Subgrid-scale backscatter in turbulent and transition flows. *Phys. Fluids* A **3**, 1766–1771.

Piomelli, U., Moin, P. & Ferziger, J. H. 1988 Model consistency in large eddy simulation of turbulent channel flows. *Phys. Fluids* **31**, 1884–1891.

Pope, S. B. 2000 *Turbulent Flows*. Cambridge University Press.

Porte-Agel, F., Meneveau, C. & Parlange, M. B. 2000 A scale-dependent dynamic model for large-eddy simulation: application to a neutral atmospheric boundary layer. *J. Fluid Mech.* **415**, 261–284.

Raupach, M. R., Antonia, R. A. & Rajagopalan, S. 1991 Rough-wall turbulent boundary layers. *Appl. Mech. Rev.* **44**, 1–25.

Roth, G. I. & Katz, J. 2001 Five techniques for increasing the speed and accuracy of PIV interrogation. *Meas. Sci. Technol.* **12**, 238–245.

Roth, G. I., Mascenik, D. T. & Katz, J. 1999 Measurements of the flow structure and turbulence within a ship bow wave. *Phys. Fluids* **11**, 3512–3523.

Saddoughi, S. G. & Veeravalli, S. V. 1994 Local isotropy in turbulent boundary layers at high Reynolds number. *J. Fluid Mech.* **268**, 333–372.

Scotti, A., Meneveau, C. & Lilly, D. K. 1993 Generalized Smagorinsky model for anisotropic grids. *Phys. Fluids* A **5**, 2306–2308.

Shaw, R. H. & Schumann, U. 1992 Large-eddy simulation of turbulent flow above and within a forest. *Boundary Layer Met.* **61**, 47–64.

Skyllingstad, E. D., Smyth, W. D., Moum, J. N. & Wijesekera, H. 1999 Upper-ocean turbulence during a westerly wind burst: a comparison of large-eddy simulation results and microstructure measurements. *J. Phys. Oceanogr.* **29**, 5–28.

Skyllingstad, E. D. & Wijesekera, H. W. 2004 Large-eddy simulation of flow over two-dimensional obstacles: high drag states and mixing. *J. Phys. Oceanogr.* **34**, 94–112.

Smagorinsky, J. 1963 General circulation experiments with the primitive equations. *Mon. Weath. Rev.* **91**, 99–164.

Snodgrass, F. E., Groves, G. W., Hasselmann, K. F., Miller, G. R., Munk, W. H. & Powers, W. H. 1966 Propagation of ocean swell across the pacific. *Phil. Trans. R. Soc. Lond.* A **259**, 431–497.

Tao, B., Katz, J. & Meneveau, C. 2002 Statistical geometry of subgrid-scale stresses determined from holographic particle image velocimetry measurements. *J. Fluid Mech.* **457**, 35–78.

Teixeira, M. A. C. & Belcher, S. E. 2002 On the distortion of turbulence by a progressive surface wave. *J. Fluid Mech.* **458**, 229–267.

Terray, E. A., Donelan, M. A., Agrawal, Y. C., Drennan, W. M., Kahma, K. K., Williams, A. J., Hwang, P. A. & Kitaigorodskii, S. A. 1996 Estimates of kinetic energy dissipation under breaking waves. *J. Phys. Oceanogr.* **26**, 792–807.

Thais, L. & Magnaudet, J. 1996 Turbulent structure beneath surface gravity waves sheared by the wind. *J. Fluid Mech.* **328**, 313–344.

Townsend, A. A. 1961 Equilibrium layers and wall turbulence. *J. Fluid Mech.* **11**, 97–120.

Trowbridge, J. H. 1998 On a technique for measurement of turbulent shear stress in the presence of surface waves. *J. Atmos. Oceanic Technol.* **15**, 290–298.